IRAQI JOURNAL OF APPLIED PHYSICS

IJAP www.iraqiphysicsjournal.com, www.facebook.com/editor.ijap, @IJAP2010

IRAQI JOURNAL OF APPLIED PHYSICS

" INSTRUCTIONS TO AUTHORS "

CONTRIBUTIONS

Contributions to be published in this journal should be original research works, i.e., those not already published or submitted for publication elsewhere, individual papers or letters to editor.
Manuscripts should be submitted to the editor at the mailing address:

Iraqi Journal of Applied Physics, Editorial Board
P. O. Box 55259, Baghdad 12001, IRAQ, admin@iraqiphysicsjournal.com, editor_ijap@yahoo.co.uk

MANUSCRIPTS

Two hard copies with soft copy on a compact disc (CD) should be submitted to Editor in the following configuration:

- **One-column** Double-spaced one-side A4 size with 2.5 cm margins of all sides
- Times New Roman font (16pt bold for title, 14pt bold for names, 12pt bold for headings, 12pt regular for text)
- Letters should not exceed 10 pages, papers should not exceed 20 pages and reviews are up to author.
- Manuscripts presented in English only are accepted.
- English abstract not exceed 150 words
- 4 keywords (at least) should be maintained on (PACS preferred)
- Author(s) should express all quantities in SI units
- Equations should be written in equation form (*italic* and symbolic)
- Figures and Tables should be separated from text
- Figures and diagrams can be submitted in colors for assessment and they will be returned to authors after provide printable copies
- Charts should be indicated by the software used for
- Only original or high-resolution scanner photos are accepted
- For electronic submission, articles should be formatted with MS-Word software.

AUTHOR NAMES AND AFFILIATIONS

It is IJAP policy that all those who have participated significantly in the technical aspects of a paper be recognized as co-authors or cited in the acknowledgments. In the case of a paper with more than one author, correspondence concerning the paper will be sent to the first author unless staff is advised otherwise.
Author name should consist of first name, middle initial, last name. The author affiliation should consist of the following, as applicable, in the order noted:
- Company or college (with department name or company division), Postal address, City, state, zip code, Country name, and Telephone, and e-mail

REFERENCES

The references should be brought at the end of the article, and numbered in the order of their appearance in the paper. The reference list should be cited in accordance with the following examples:
[1] X. Ning and M.R. Lovell, "On the Sliding Friction Characteristics of Unidirectional Continuous FRP Composites", *ASME J. Tribol.*, 124(1) (2002) 5-13.
[2] M. Barnes, "Stresses in Solenoids", *J. Appl. Phys.*, 48(5) (2001) 2000–2008.
[3] J. Jones, "Contact Mechanics", Cambridge University Press (Cambridge, UK) (2000), Ch.6, p.56.
[4] Y. Lee, S.A. Korpela and R. Horne, "Structure of Multi-Cellular Natural Convection in a Tall Vertical Annulus", Proc. 7th International Heat Transfer Conference, U. Grigul et al., eds., Hemisphere (Washington DC), 2 (1982) 221–226.
[5] M. Hashish, "Waterjet Technology Development", High Pressure Technology, PVP-Vol. 406 (2000), 135-140.
[6] D.W. Watson, "Thermodynamic Analysis", ASME Paper No. 97-GT-288 (1997).
[7] C.Y. Tung, "Evaporative Heat Transfer in the Contact Line of a Mixture", Ph.D. thesis, Rensselaer Polytechnic Institute, Troy, NY (1982).

PROOFS

Authors will receive proofs of papers and are requested to return one corrected hard copy with a WORD copy on a compact disc (CD). New materials inserted in the original text without Editor permission may cause rejection of paper.

COPYRIGHT FORM

Author(s) will be asked to transfer copyrights of the article to the Journal soon after acceptance of it. This will ensure the widest possible dissemination of information.

OFFPRINTS

Authors will receive offprints free of charge and any additional offprints can be ordered.

SUBSCRIPTION AND ORDERS

Annual fees (4 issues per year) of subscription are:
- 50 US$ for individuals inside Iraq.
- 100 US$ for establishments inside Iraq.
- 100 US$ for individuals abroad.
- 200 US$ for establishments abroad.

Fees are reduced by 25% for I.S.A.R.E.S.T. members. Orders of issues can be submitted by contacting the editor-in-chief or editorial office at **admin@iraqiphysicsjournal.com** or **editor_ijap@yahoo.co.uk** to maintain the address of issue delivery and payment way.

Parallelized Chromatic Confocal Systems Enable Efficient Spectral Information Coding

Matthias Hillenbrand
Adrian Grewe
Stefan Sinzinger

Institute for Micro- and Nanotechnologies (IMN MacroNano) Ilmenau University of Technology Ilmenau, Germany

Parallelized imaging systems based on the chromatic confocal approach can be used for hyperspectral imaging and optical profilometry.

Chromatic confocal imaging systems[1–3] are based on the well-known principle of confocal microscopy.[4] They use a polychromatic light source instead of a laser, and the focal length has strong wavelength dependence so that different wavelengths are focused at different axial distances. The wavelength dependence is achieved by replacing the standard objective lens with a hyperchromatic lens.[5, 6] Hyperchromatic systems are characterized by an optimized longitudinal chromatic aberration adapted to the specific application requirements.[7, 8]

The chromatic confocal approach can be used in various system concepts for chromatic information encoding and decoding. Currently, we are mainly working on parallelized systems for chromatic confocal distance sensing (profilometry) and hyperspectral imaging.[6, 9–11] Hyperspectral imaging combines spatially and spectrally resolved imaging to detect the full spectral signature of the analyzed object. Typical applications include agriculture, geology, mineralogy, and surveillance.

To use a hyperchromatic lens for chromatic information coding, optically conjugate pinhole arrays are placed in the object and image space of the lens (see Figure 1). The object-space pinhole array transforms the polychromatic object information or the illumination beam into a number of spatially separated quasi-point sources.
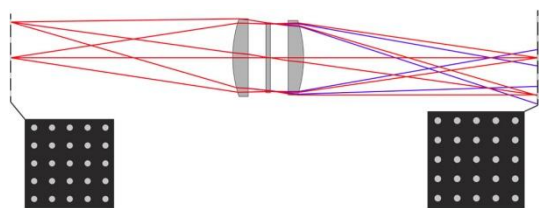
Figure 1. *Chromatic information coding system. A hyperchromatic lens (depicted by the central three elements) separates the spectral components along the direction of light propagation. Pinhole arrays in the lens's object space (at left) and image space (at right) filter the spectral content of the signal.*

When the hyperchromatic lens images these polychromatic point sources, their spectral components become separated along the direction of light propagation. The image-space pinhole array is placed within this focal range and attenuates all wavelengths except the one in focus at the pinhole plane. Thus, the spectral signals passing the pinhole plane show a significant peak for this specific wavelength.

The longitudinal chromatic aberration required by chromatic confocal systems may be created with refractive systems, diffractive systems, or hybrid combinations of diffractive and refractive elements. Because the longitudinal chromatic aberration caused by a diffractive optical element (DOE) is six to 25 times larger than that achieved with a refractive component of the same focal length, DOEs are very well suited for use in chromatic confocal systems.[12] They enable an efficient correction of monochromatic aberrations through an aspherical phase function, but they are also linked to various challenges such as a limited diffraction efficiency. By balancing the powers of the diffractive and refractive components, the spectral sensor characteristics can be tailored to the specific measurement problem.[6]

We use a two-stage design approach to develop application-specific chromatic confocal systems. During the first stage, we apply a collinear model to define the system layout. At this point, the main performance criteria (such as the spatial and spectral resolution) and the field and the system size are determined by the choice of the collinear system parameters. Among the most important parameters relevant to chromatic confocal systems are the numerical aperture, the longitudinal chromatic aberration, the pinhole diameter and spacing, and the lateral magnification. By an appropriate choice of these parameters, subnanometer spectral resolution can be reached.[9] During the second stage, we use an optimization process based on ray tracing to cope

with the on-axis and field-dependent monochromatic aberrations. For optimum performance, these aberrations must be corrected over the full spectral range of the optical system.

Figure 2. *Chromatic confocal single-pass system for hyperspectral imaging.*[9]

We have used these techniques to design a single-pass chromatic confocal system for hyperspectral imaging (see Figure 2). To provide the quasi-point sources necessary for the chromatic confocal approach, the object scene is imaged onto the first pinhole array. A telecentric hyperchromatic lens system then separates the spectral information along the axis. We can select the spectral channels of interest by tuning the focal length of the hyperchromatic system or by moving the detector system axially. Thus, we co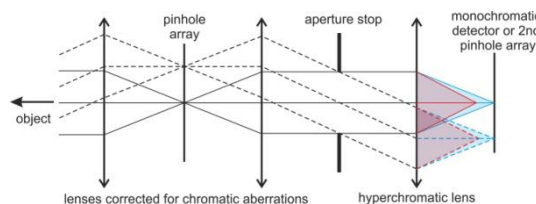mbine a parallelized readout of the spatial channels with a sequential evaluation of the spectral channels, which may reach subnanometer bandwidths. Tuning concepts for the hyperchromatic group include classical zoom systems, adaptive mirrors, fluidic membrane lenses, and Alvarez-Lohmann lenses.[11, 13,14]
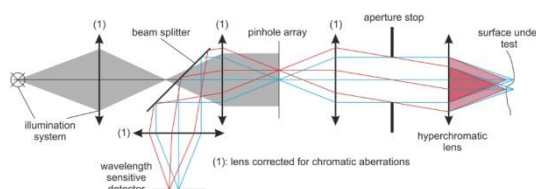

Figure 3. *Chromatic confocal double-pass system for parallelized evaluation of an extended object.*[9]

For chromatic confocal distance sensing, we use a double-pass system (see Figure 3). A polychromatic light source illuminates the pinhole array to create an array of quasi-point sources. The hyperchromatic lens focuses the spectral components of these point sources at different distances. If a reflecting or scattering surface is brought within the measurement range, for each pinhole only one specific wavelength will be in focus on the surface, according to the axial distance to the surface at that spot. The reflected or scattered light of this specific focus will also be in focus on the pinhole plane. It will pass the pinhole plane, whereas all other wavelengths will be defocused and

strongly attenuated. By evaluating the wavelength of the spectral peaks, the shape and distance of the surface can be determined in parallel for all points of the pinhole array.

In summary, we have designed optimized parallelized chromatic confocal systems for conducting hyperspectral imaging and optical profilometry. Our current work on hyperspectral imaging is focused on the development of miniaturized, application-specific sensor systems. For this purpose, we are integrating actuators based on microelectromechanical systems (MEMS) to tune the focus of Alvarez-Lohmann lenses and to enhance the lateral resolution through a lateral movement of the pinhole arrays. The next step in our optical profilometry work will address the challenging task of performing the parallelized spectral evaluation of all the measurement points. To this end, we are working on a novel snapshot sensor that combines an array-based chromatic confocal setup with a hyperspectral detection system to enable measurement of the full surface topography with a single shot.

References
1. G. Molesini, G. Pedrini, P. Poggi, F. Quercioli, Focus-wavelength encoded optical profilometer, *Opt. Commun.* 49, p. 229-233, 1984.
2. M. A. Browne, O. Akinyemi, A. Boyde, Confocal surface profiling utilizing chromatic aberration, *Scanning* 14, p. 145-153, 1992.
3. H. J. Tiziani, H.-M. Uhde, Three-dimensional image sensing by chromatic confocal microscopy, *Appl. Opt.* 33, p. 1838-1843, 1994.
4. T. Wilson, C. Sheppard, *Theory and Practice of Scanning Optical Microscopy*, Academic Press, London, 1985.
5. J. Novak, A. Miks, Hyperchromats with linear dependence of longitudinal chromatic aberration on wavelength, *Optik* 116, p. 165-168, 2005.
6. M. Hillenbrand, B. Mitschunas, C. Wenzel, A. Grewe, X. Ma, P. Feßer, M. Bichra, S. Sinzinger, Hybrid hyperchromats for chromatic confocal sensor systems, *Adv. Opt. Technol.* 1, p. 187-194, 2012.
7. R. Kingslake, R. B. Johnson, *Lens Design Fundamentals*, Academic Press, Boston, 2010.
8. H. Haferkorn, *Bewertung Optischer Systeme*, Dt. Verl. d. Wiss, Berlin, 1985.
9. M. Hillenbrand, A. Grewe, M. Bichra, B. Mitschunas, R. Kirner, R. Weiß, S. Sinzinger, Chromatic information coding in optical systems for hyperspectral imaging and chromatic confocal sensing, *Proc. SPIE* 8550, p. 85500D, 2013.
10. M. Hillenbrand, C. Wenzel, X. Ma, P. Feßer, S. Sinzinger, Hyperchromatic confocal sensor systems, *Proc. 8th EOS Top. Mtg. Diffractive Opt.*, p. 4847, 2012.
11. A. Grewe, M. Hillenbrand, S. Sinzinger, Adaptive confocal approach to hyperspectral imaging, *Proc. EOSAM 2012*, p. 6081, 2012.
12. J. Garzón, D. Duque, A. Alean, M. Toledo, J. Meneses, T. Gharbi, Diffractive elements performance in chromatic confocal microscopy, *J. Phys.: Conf. Ser.* 274, p. 012069, 2011.
13. L. W. Alvarez, W. E. Humphrey, Variable-power lens and system, *US Patent* 3,507,565, 1970.
14. A. W. Lohmann, A new class of varifocal lenses, *Appl. Opt.* 9, p. 1669-1671, 1970.
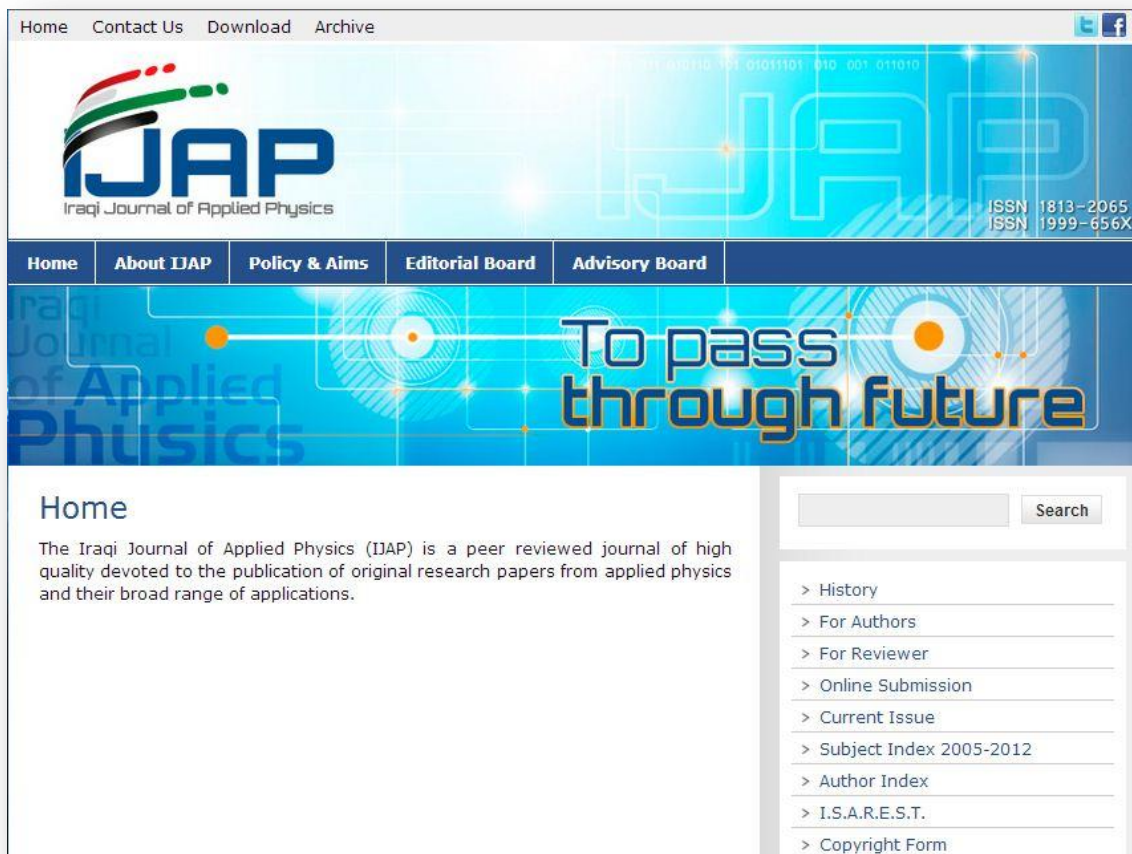
| Home | About IJAP | Policy & Aims | Editorial Board | Advisory Board |

Iraqi Journal of Applied Physics

To pass through future

I.S.A.R.E.S.T.

Iraqi Society for Alternative and Renewable Energy

Congratulations on the successful accomplishment of the I.S.A.R.E.S.T. formation. The association by the blessings of Allah Almighty and the joint efforts of Founder Members has become the first legal entity of Alternative and Renewable Energy in Iraq. The credit goes to you all (Founding Members) who honored our call to uplift our country from current energy crises and by committing to promote Alternate Energy in the country.

We are thankful to honor our request and on behalf of The Board; we recompense our especial thanks for all those who expressed their confidence on the abilities of the entire team.

We would like to take the opportunity to commit that the Board will not leave any stone unturned to fulfill our expectations. Our main focus is to break the barrier of awareness about Alternative and Renewable Energy in the country and we need you all to please work together to cross this milestone.

Best regards,
President I.S.A.R.E.S.T.
Baghdad, Headquarter

| | Search |

> History
> For Authors
> For Reviewer
> Online Submission
> Current Issue
> Subject Index 2005-2012
> Author Index
> I.S.A.R.E.S.T.
> Copyright Form
> Sponsors and Partners
> Events and News

Online Submission

Comments or questions are welcome.

*(denotes required field)

First Name: *

Middle Name:

Last Name: *

E-Mail Address: *

Affiliation

Contact Address

Co-Author (1)

Affiliation

Co-Author (2)

Affiliation

Title of Article

Abstract

Keywords

Date
mm/dd/yyyy

Upload files
Choose File   No file chosen
Acceptable file types: docx,doc,pdf,txt,gif,jpg,jpeg,png.
Maximum file size: 1mb.

CAPTCHA Code: *

Submit

Sphoorti Srivastava [1]
Neeraj Mehta [2]
Deepak Kumar [3]
Ashok Kumar [1]

[1] *Department of Physics, Harcourt Butler Technological Institute, Kanpur – 02, INDIA*
[2] *Department of Physics, Banaras Hindu University, Varanasi, India*
[3] *Department of Physics, J. S. S. Academy of Technical Education, Noida, INDIA*

Crystallization and Glass Transition Kinetics in Se$_{90}$Sb$_{10-x}$Ag$_x$ Glassy Alloys

Alloys of Se$_{100-x}$Sb$_{10-x}$Ag$_x$ (x=2, 4, 8) glassy system are obtained with rapid quenching. Calorimetric studies have been performed at different heating rates under non-isothermal conditions. Well defined endothermic and exothermic peaks are obtained at glass transition (T$_g$) and crystallization temperatures (T$_c$). In the present study, the glassy alloys are found to have double glass transition and crystallization temperatures. From the dependence of the glass transition temperature on the heating rate β, the activation energy of glass transition has been calculated on the basis of Moynihan and Kissinger models. The value of (T$_c$–T$_g$) and stability parameters have also been calculated for each composition for both the phases. Value of E$_g$ is found to be decreased with increase in concentration of Ag. The values of (T$_c$-T$_g$) is highest for the sample with 8 at % of Ag. Activation energy of crystallization (E$_c$) has also been calculated using the well-known Kissinger's relation, Matusita–Sakka theory and the method of Augis and Bennett. A good agreement has been found in all the three methods. The activation energy of crystallization is found to decrease with increasing concentration of Ag.

1. Introduction

Differential Scanning Calorimetery (DSC) is more sensitive than other thermoanalytical technique, Differential Thermal Analysis (DTA), and measures the volume fraction transferred as a function of time and temperature by measuring the heat liberated or absorbed during the phase change. The study of crystallization kinetics using DSC has been widely discussed in the literature [1 - 5]. DSC is widely used to study the dependence of glass transition temperature (T$_g$) and crystallization temperature (T$_c$) on the particle size, composition and heating rate. From the heating rate dependence of glass transition and crystallization temperatures the activation energies of glass transition and crystallization are calculated. Thermally activated transformations in the solid state can be investigated by isothermal or non-isothermal experiments [6 - 8]. In the isothermal method, the sample is brought quickly to a temperature above T$_g$ and the heat evolved during the crystallization process is recorded as a function of time. Compared with isothermal techniques, non-isothermal experiments can be performed over a shorter time period and over a wider temperature range. In addition many phase transformations occur too rapidly to be measured under isothermal conditions because of the inherent transients associated with the experimental apparatus [6]. In the non-isothermal method, the sample is heated at a fixed rate and the heat evolved is again recorded as a function of temperature or time. A constant heating rate method (non-isothermal method) does not have the drawback of isothermal method [9], i.e., the impossibility of reaching a test temperature instantaneously and during the time in which the system needs to stabilize no measurements are possible. In general, therefore, crystallization studies have been made under non-isothermal conditions with the sample heated at several uniform heating rates. So, in the present study also, an effort has been made to determine the activation energies of glass transition and crystallization by using heating rate dependence of the T$_g$ and T$_c$.

Thin films of chalcogenide glasses containing Ag have found application in erasable PC optical recording [10-15]. Different Ag doped chalcogenide alloys have been developed as recording layer and their good practical performance have been reported [10-15]. The electrical, optical and structural properties of Ag doped chalcogenide glasses have been studied by various workers [16-25] but there are only a few studies reported on crystallization kinetics in these materials [26-28].

Generally, silver containing chalcogenide glasses, exhibit single glass transition and single crystallization temperature, but in the present study the glassy alloys of Se$_{90}$Sb$_{10-x}$Ag$_x$ (x=2, 4, 8) are found to have double glass transition and crystallization temperatures. Therefore, crystallization kinetics of these glassy alloys has been studied in detail for both the phases present in these alloys.

2. Experimental Procedure

Glassy alloys of Se$_{90}$Sb$_{10-x}$Ag$_x$ (x=2, 4, 8) were prepared by quenching technique. The exact proportions of high purity (99.999%) elements, in

accordance with their atomic percentages, were weighed using an electronic balance (LIBROR. AEG -120), with the least count 10^{-4} mg. The materials were then sealed in evacuated ($\sim 10^{-5}$ torr) quartz ampoules (length ~ 5cm and internal diameter ~ 8mm). Each ampoule was kept inside the furnace at 1000°C temperature (where the temperature was raised at a rate of 3-4°C/min.). During heating, all the ampoules were constantly rocked by rotating a ceramic rod to which the ampoules were tucked away in the furnace. This was done to obtain homogeneous glassy alloys.

After rocking for about 10 hours, the obtained melts were cooled rapidly by removing them from the furnace and dropping them to ice-cooled water rapidly. The ingots of the samples were then taken out by breaking the quartz ampoules.

The glasses thus prepared, were ground to make fine powder for DSC studies. Here, 10 to 20 mg of the powder was heated at constant heating rate and the changes in heat flow with respect to an empty reference pan were measured. DSC plus instrument (Rheometric Scientific Company, U.K.) was used at four different heating rates of 5, 10, 15 and 20°C/min.

3. Results and Discussion

Figures (1) and (2) show typical DSC thermograms for glassy $Se_{90}Sb_{10-x}Ag_x$ (x=2, 4 and 8) at heating rate 15 K/min. Similar thermograms were obtained for other heating rates also (not shown here). These figures indicate that two phases occur simultaneously during glass transition region and crystalline transition region.
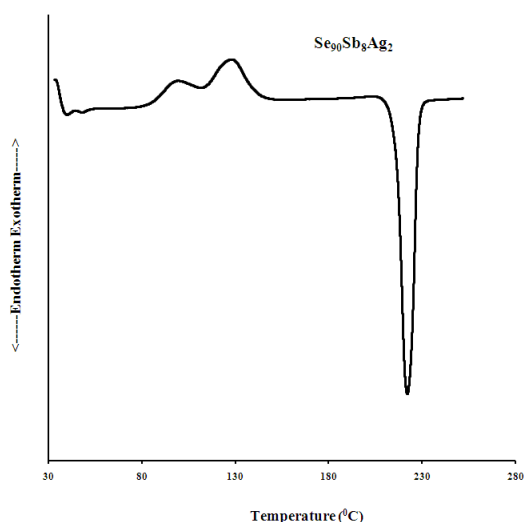
Fig. (1) DSC thermogram for glassy $Se_{90}Sb_8Ag_2$ alloy for heating rate 15°C/min

3.1 Composition Dependence of Glass Transition and Crystallization Temperature

Tables (1) and (2) give the values of glass transition temperature for different compositions at various heating rates. From the given data it is clear that glass transition temperature increases with Ag concentration for phase two. However, for phase one there is no drastic change in T_g with composition.
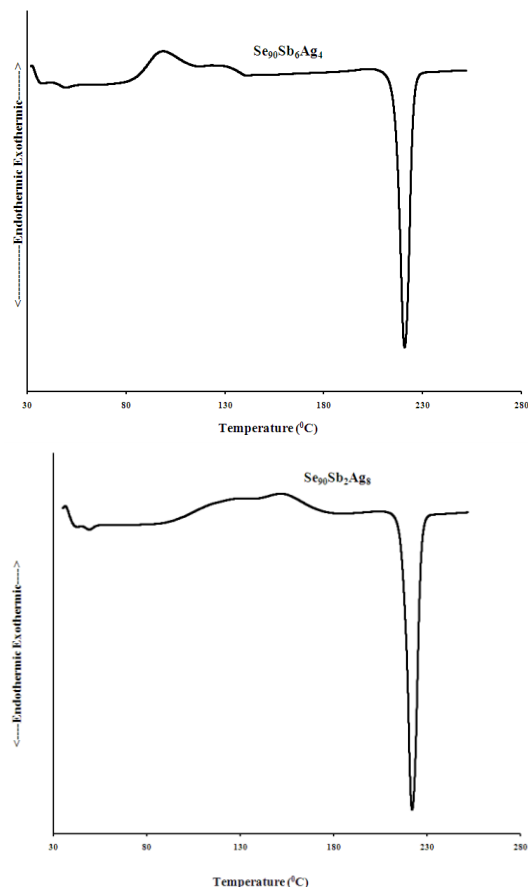
Fig. (2) DSC thermogram for glassy $Se_{90}Sb_6Ag_4$ and $Se_{90}Sb_2Ag_8$ alloy for heating rate 15°C/min

Table (1) Glass transition temperature T_{g1} at different heating rates for phase 1

Heating rate	$Se_{90}Sb_8Ag_2$	$Se_{90}Sb_6Ag_4$	$Se_{90}Sb_2Ag_8$
5 K/min	309.69	309.53	307.01
10 K/min	312.01	312.15	311.53
15 K/min	313.06	310.8	315.64
20 K/min	313.30	314.7	313.11

Table (2) Glass transition temperature T_{g2} at different heating rates for phase 2

Heating rate	$Se_{90}Sb_8Ag_2$	$Se_{90}Sb_6Ag_4$	$Se_{90}Sb_2Ag_8$
5 K/min	317.69	318.35	318.61
10 K/min	318.99	320.12	320.95
15 K/min	321.06	322.58	322.19
20 K/min	323.19	323.43	324.17

Tables (3) and (4) give the variation of crystallization temperature for different

compositions at various heating rates. It is clear from these tables that crystallization temperature increases with the increase in heating rate. These values are also composition dependent.

Table (3) Crystallization temperature T_{c1} at different heating rates for phase 1

Heating Rate	$Se_{90}Sb_8Ag_2$	$Se_{90}Sb_6Ag_4$	$Se_{90}Sb_2Ag_8$
5^0C/min	363.04	360.75	401.23
10^0C/min	366.98	367.33	414.41
15^0C/min	372.46	371.66	402.73
20^0C/min	373.92	374.13	404.70

Table (4) Crystallization temperature T_{c2} at different heating rates for phase 2

Heating Rate	$Se_{90}Sb_8Ag_2$	$Se_{90}Sb_6Ag_4$	$Se_{90}Sb_2Ag_8$
5^0C/min	388.51	391.28	---
10^0C/min	393.52	396.45	---
15^0C/min	401.09	397	424.62
20^0C/min	397.75	397.93	431.37

3.2 Activation Energy of Glass Transition

The evaluation of activation energy of glass transition (E_g) from the heating rate dependence of glass transition temperature is widely used in the literature. The theory of glass transition kinetics and structural relaxation as developed by Moynihan and other workers [29-31] has been used for this purpose. According to this theory, T_g and heating rate β are related as per the following equation:

$$\frac{d\,Ln\beta}{d\left(\frac{1}{T_g}\right)} = -\frac{E_g}{R} \qquad (1)$$

According to Eq. (1), the ln β versus $1/T_g$ plot should be a straight line and the activation energy involved in the molecular motions and rearrangements around T_g can be calculated from the slope of the plot of ln β vs. $10^3 / T_g$.

Kissinger's method is most commonly used in analyzing crystallization data of DSC experiment. Kissinger showed that:

$$Ln\left(\frac{\beta}{T_c^2}\right) = Constant - \frac{E_c}{RT_c} \qquad (2)$$

where T_c is peak crystallization temperature

Although originally derived for the crystallization process, it is suggested that this relation is valid for glass transition process [32 - 33] also and hence the above equation takes the following form for its use in glass transition kinetics:

$$Ln\left(\frac{\beta}{T_g^2}\right) = -\frac{E_g}{RT_g} + Constant \qquad (3)$$

Using Moynihan's relation, equation (1), the plots of ln β against $10^3/T_g$ are plotted for various glassy alloys. These plots are shown in Figs. (3-8) for various glassy alloys of $Se_{90}Sb_{10-x}Ag_x$ (x=2, 4, 8). The slopes of these plots are used to calculate the

activation energy of glass transition process. Tables (5) and (6) show the E_g values obtained from Eq. (1). The values of E_g are also evaluated from the slopes of plots of ln (β/T_g^2) against $10^3/T_g$ for various glassy systems using Kissinger's relation, i.e., Eq. (3). The plots of ln (β/T_g^2) vs. $1000 / T_g$ are also shown in Figs. (3-8) for glassy alloys of $Se_{90}Sb_{10-x}Ag_x$ (x=2, 4, 8). These values of E_g are given in Tables (5) and (6) for both phases.
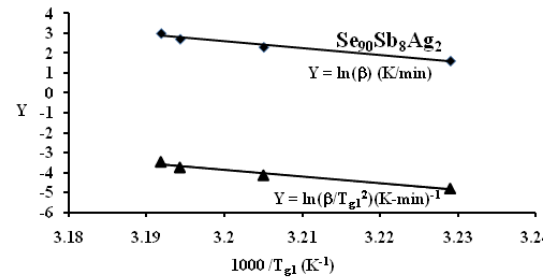
Fig. (3) Plots of ln(β/T_{g1}^2), ln(β) against $10^3/T_{g1}$ for $Se_{90}Sb_8Ag_2$
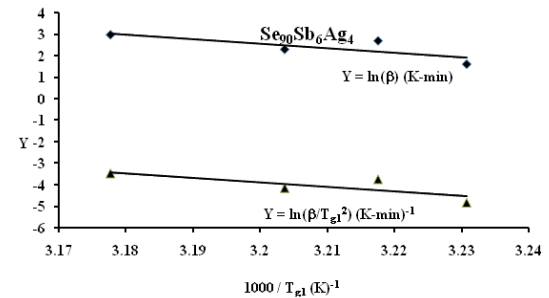

Fig. (4) Plots of ln(β/T_{g1}^2), ln(β) against $10^3/T_{g1}$ for $Se_{90}Sb_6Ag_4$
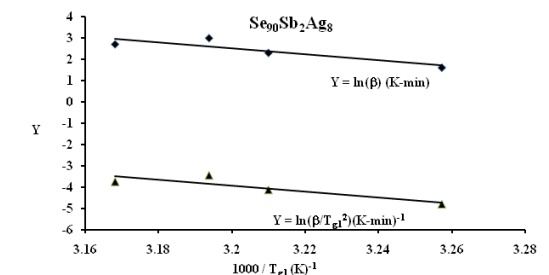

Fig. (5) Plots of ln(β/T_{g1}^2), ln(β) against $10^3/T_{g1}$ for $Se_{90}Sb_2Ag_8$
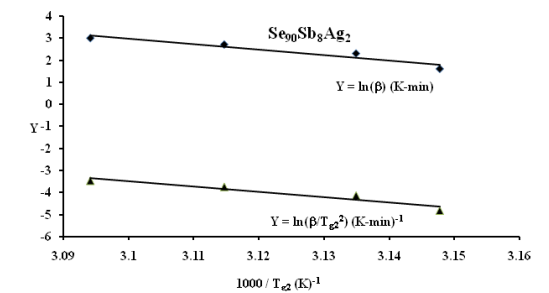
Fig. (6) Plots of ln(β/T_{g2}^2), ln(β) against $10^3/T_{g2}$ for $Se_{90}Sb_8Ag_2$
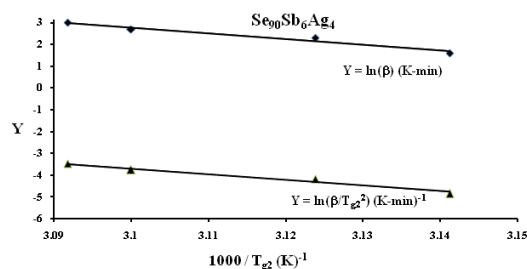
Fig. (7) Plots of ln(β/T$_{g2}^2$), ln(β) against 10^3/T$_{g2}$ for Se$_{90}$Sb$_6$Ag$_4$
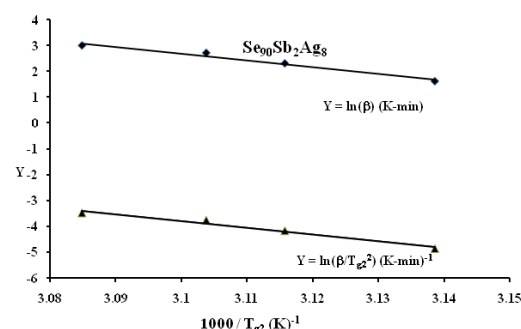
Fig. (8) Plots of ln(β/T$_{g2}^2$), ln(β) against 10^3/T$_{g2}$ for Se$_{90}$Sb$_2$Ag$_8$

It is evident from the Tables (5) and (6) and Figs. (9) and (10) that E$_g$ varies with Ag concentration and decreases as Ag concentration increases. It can be explained in terms of atomic weights of Sb and Ag. The atomic weight of Ag (107.87 gm/mol) is much less than that of Sb (121.75 gm/mol). In the present case, Ag is added in binary Se$_{90}$Sb$_{10}$ at the cost of Sb. Thus, the mean atomic weight of ternary alloys is decreased. This may probably be the reason why activation energy of glass transition is lower as Ag concentration increases.

Table (5) Activation Energy of glass transition E$_{g1}$ (eV) for various glassy alloys of Se$_{90}$Sb$_{10-x}$Ag$_x$ for phase 1

Sample	Moynihan's relation	Kissinger's relation
Se$_{90}$Sb$_8$Ag$_2$	1.96	1.93
Se$_{90}$Sb$_6$Ag$_4$	1.82	1.79
Se$_{90}$Sb$_2$Ag$_8$	1.22	1.19

Table (6) Activation Energy of glass transition E$_{g2}$ (eV) for various glassy alloys of Se$_{90}$Sb$_{10-x}$Ag$_x$ for phase 2

Sample	Moynihan's relation	Kissinger's relation
Se$_{90}$Sb$_8$Ag$_2$	1.99	1.96
Se$_{90}$Sb$_6$Ag$_4$	1.89	1.86
Se$_{90}$Sb$_2$Ag$_8$	1.79	1.77

Table (7) Values of T$_{c1}$–T$_{g1}$ for various glassy alloys of Se$_{90}$Sb$_{10-x}$Ag$_x$

Heating Rate	Se$_{90}$Sb$_8$Ag$_2$	Se$_{90}$Sb$_6$Ag$_4$	Se$_{90}$Sb$_2$Ag$_8$
5^{0}C/min	53.35	51.22	94.22
10^{0}C/min	56.89	55.18	99.58
15^{0}C/min	58.4	60.86	88.09
20^{0}C/min	60.84	59.43	92.88

Table (8) Values of T$_{c2}$–T$_{g2}$ for various glassy alloys of Se$_{90}$Sb$_{10-x}$Ag$_x$

Heating Rate	Se$_{90}$Sb$_8$Ag$_2$	Se$_{90}$Sb$_6$Ag$_4$	Se$_{90}$Sb$_2$Ag$_8$
5^{0}C/min	72.02	71.93	-
10^{0}C/min	75.53	77.65	-
15^{0}C/min	77.95	72.42	101.20
20^{0}C/min	73.56	75.50	106.97
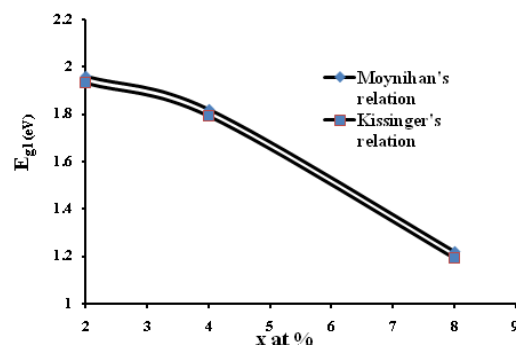
Fig. (9) E$_{g1}$ vs. atomic percentage of Ag in glassy Se$_{90}$Sb$_{10-x}$Ag$_x$
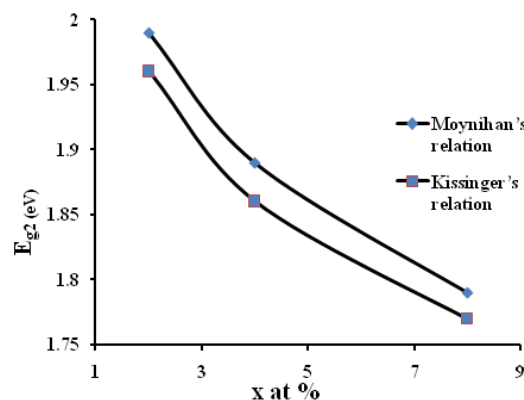
Fig. (10) E$_{g2}$ vs. atomic percentage of Ag in glassy Se$_{90}$Sb$_{10-x}$Ag$_x$

3.3 Thermal Stability of Glassy Se$_{90}$Sb$_{10-x}$Ag$_x$ (x=2, 4, 8)

It has been found that the difference of T$_c$ and T$_g$ is a strong indicator of both the thermal stability and GFT. The higher the values of (T$_c$-T$_g$), the greater is the GFT, because the higher the value of this difference, the more the delay in the nucleation process [34]. Tables (1-4) show the glass transition and crystallization temperature T$_c$ at various heating rates for phase one and two in all the glasses studied. Values of difference of glass transition temperature (T$_g$) and crystallization temperature (T$_c$) are given in Tables (9) and (10) for both the phases. Figures (11) and (12) show the variation of (T$_c$-T$_g$) with concentration of Ag for both phases. It is clear that (T$_c$-T$_g$) increases with Ag concentration. This indicates that thermal stability is higher at higher concentration of Ag.

Table (9) Activation energy of crystallization E_{c1}(eV) in various glassy alloys of $Se_{90}Sb_{10-x}Ag_x$

Non-isothermal Method	$Se_{90}Sb_8Ag_2$	$Se_{90}Sb_6Ag_4$	$Se_{90}Sb_2Ag_8$
Augis Bennett's Method	1.35	1.16	0.66
Matusita and Sakka's method	1.38	1.19	0.71
Kissinger's Method	1.35	1.16	0.66

Table (10) Activation energy of crystallization E_{c2}(eV) in various glassy alloys of $Se_{90}Sb_{10-x}Ag_x$

Non-isothermal Method	$Se_{90}Sb_8Ag_2$	$Se_{90}Sb_6Ag_4$	$Se_{90}Sb_2Ag_8$
Augis Bennett's Method	1.80	1.71	-
Matusita and Sakka's method	1.85	1.70	-
Kissinger's Method	1.80	1.71	-
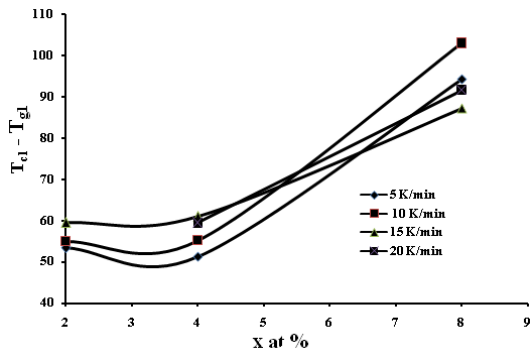
Fig. (11) $T_{c1}-T_{g1}$ vs. atomic percentage of Ag in glassy $Se_{90}Sb_{10-x}Ag_x$
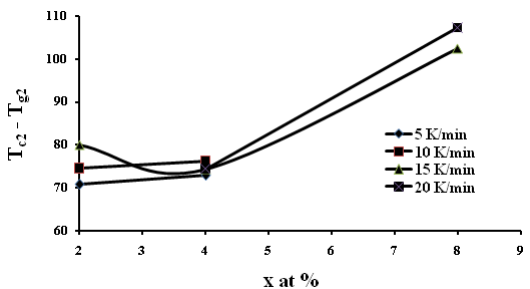
Fig. (12) $T_{c2}-T_{g2}$ vs. atomic percentage of Ag in glassy $Se_{90}Sb_{10-x}Ag_x$

3.4 Activation Energy of Crystallization Kinetics

The activation energy of crystallization of each alloy has been calculated by three different methods Kissinger's method, Matusita-Sakka & Augis and Bennett used in the literature. According to Kissinger [35], peak temperature of crystallization T_c in terms of the heating rate β, can be expressed as:

$$Ln\left(\frac{\beta}{T_c^2}\right) = -\frac{E_c}{RT_c} + Constant \qquad (4)$$

This equation is used to calculate the activation energy of crystallization by plotting ln β/T_c^2 vs. $10^3/T_c$ curves (Figs. 13-17). Values calculated are given in Tables (9) and (10).

For the evaluation of E_c, Matusita and Sakka [36, 37] derived the following relation using the classical JMA theory:

$$Ln\beta = -\frac{E_c}{RT_c} + Constant \qquad (5)$$

This equation is used to calculate the activation energy of crystallization by plotting ln β vs. $10^3/T_c$ curve (Figs. 13-17). Values calculated are given in Tables (9) and (10).
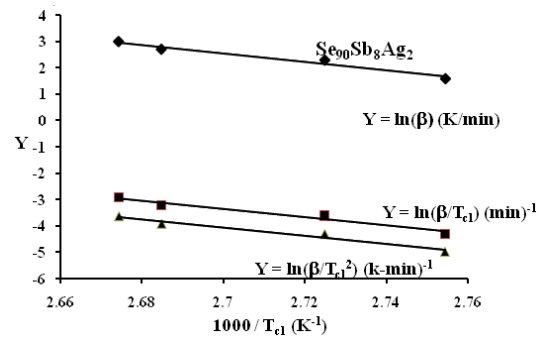
Fig. (13) Plots of ln (β/T_{c1}^2), ln (β/T_{c1}), ln (β) against $10^3/T_{c1}$ for $Se_{90}Sb_8Ag_2$
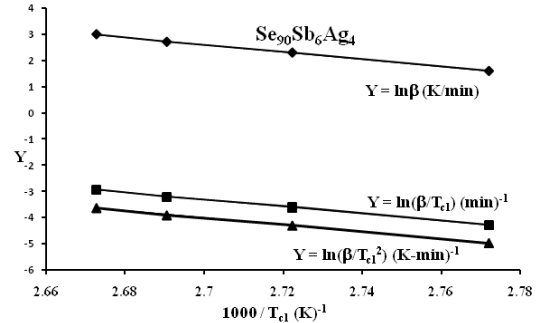
Fig. (14) Plots of ln (β/T_{c1}^2), ln (β/T_{c1}), ln (β) against $10^3/T_{c1}$ for $Se_{90}Sb_6Ag_4$
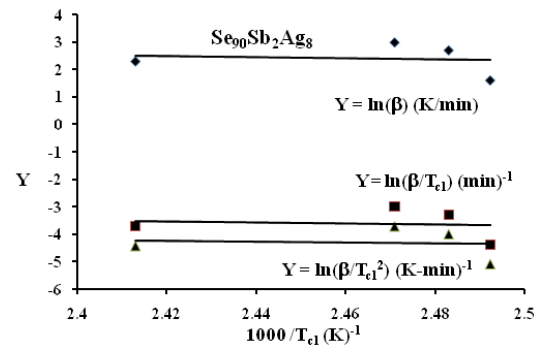
Fig. (15) Plots of ln (β/T_{c1}^2), ln (β/T_{c1}), ln (β) against $10^3/T_{c1}$ for $Se_{90}Sb_2Ag_8$
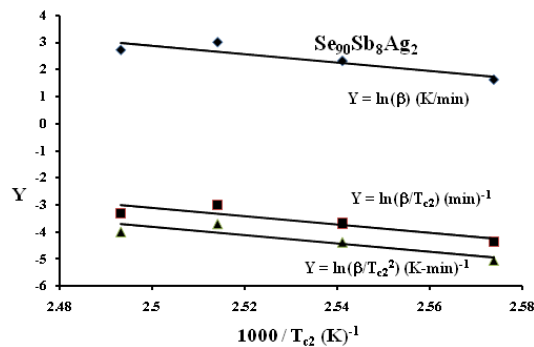
Fig. (16) Plots of ln (β/T_{c2}^2), ln (β/T_{c2}), ln (β) against $10^3/T_{c2}$ for $Se_{90}Sb_8Ag_2$
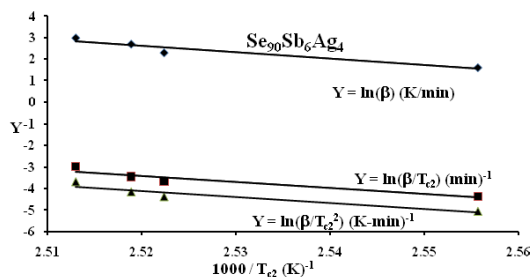
Fig. (17) Plots of ln (β/T_{c2}^2), ln (β/T_{c2}), ln (β) against $10^3/T_{c2}$ for $Se_{90}Sb_6Ag_4$

The activation energy of crystallization E_c can also be determined by an approximation method developed by Augis and Bennett [38]. The relation used by them is of the form:

$$Ln\left(\frac{\beta}{T_c}\right) = -\frac{E_c}{RT_c} + LnK_0 \qquad (6)$$

The activation energy of crystallization has been evaluated by this equation using the plots of ln β/T_c against $10^3/T_c$, as shown in Figs. (13-17). Values calculated are given in Tables (9) and (10).

Comparison of the E_c values, obtained from the three methods, shows that the values are in good agreement with each other. This means that one can use any of the three methods to obtain the activation energy of crystallization. The average value of E_{c1} and E_{c2} for each alloy has been given in the Tables (11) and (12). Figure (18) shows variation of E_{c1} with concentration of Ag.

Table (11) Average value of the activation energy of crystallization E_{c1}(eV) for various glassy alloys of $Se_{90}Sb_{10-x}Ag_x$

$Se_{90}Sb_8Ag_2$	1.36
$Se_{90}Sb_6Ag_4$	1.17
$Se_{90}Sb_2Ag_8$	0.68

Table (12) Average value of the activation energy of crystallization E_{c2} (eV) for various glassy alloys of $Se_{90}Sb_{10-x}Ag_x$

$Se_{90}Sb_8Ag_2$	1.82
$Se_{90}Sb_6Ag_4$	1.71
$Se_{90}Sb_2Ag_8$	-
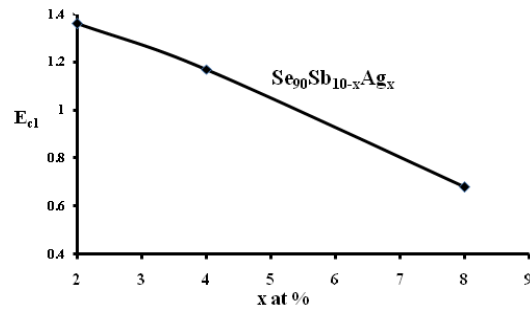
Fig. (18) E_{c1} vs. atomic percentage of Ag in glassy $Se_{90}Sb_{10-x}Ag_x$

4. Conclusion

DSC measurements have been performed for glassy alloys of $Se_{90}Sb_{10-x}Ag_x$. DSC scans of these alloys show double peaks at glass transition region as well as in crystallization region. Activation energy of glass transition E_g has been calculated by Moynihan's relation and Kissinger's relation. There is a good agreement between two values obtained from both the methods. Value of E_g is found to be decreased with increase in concentration of Ag.

The values of (T_c-T_g) is highest for the sample with 8 at % of Ag, Hence, one can conclude that the activation energy of glass transition process is related to thermal stability and GFT. Other workers have also found that the stable glass requires less activation energy for glass transition process [2, 36].

Activation energy of crystallization (E_c) has been calculated using three different methods. It has been found that E_c values obtained using the three different methods, i.e., Kissinger's method, Augis and Bennett's approximation method and Matusita and Sakka's method are in good agreement with each other. Thus one can use any of the three methods to calculate activation energy of crystallization. The activation energy of crystallization is found to decrease with increasing concentration of Ag.

References

[1] Moharram, A. H., Abu El-Oyoun, M., *J. Phys. D: Appl. Phys.*, Vol.33, (2000) pp.700.

[2] Moharram, A. H., Rasheedy, M. S., *Phys. Stat. Sol. A*, Vol.169,(1998) pp.33.

[3] Qun Gao, Yi, Wang, W., *J. Non-Cryst. Solids*, Vol. 81, (1986) pp.129.

[4] Ligero, R. A., Vazquez, J., Villares, P., Jimenez-Garay, R., *Thermochim. Acta*, Vol.162, (1990) pp.427.

[5] Abdel-Rahim, M. A., *Physica B*, Vol.239, (1997) pp.238.

[6] Rysava, N., Spasov, T., Tichy, L., *J. Thermal Anal.*, Vol. 32, (1987) pp.1015.

[7] Giridhar, A., Mahadevan, S., *J. Non-Cryst. Solids*, Vol.51, (1982) pp.305.

[8] Afify, N., *J. Non-Cryst. Solids*, Vol.128, (1991) pp.279.

[9] Strink, M. J., Zahara, A. M., *Thermochim. Acta*, Vol.298, (1997) pp.179.

[10] Chang, Y.Y., Chou, L.H., *Jpn. J. Appl. Phys. Part 2*, Vol.39 (4A), (2000) pp.294–296.

[11] Zhou, G.F., *Mater. Sci. Eng. A* , Vol.304–A306, (2001) pp.73.

[12] Chou, L.H., Chang, Y.Y., Chai, Y.C., Wang, S.Y., *J. Appl. Phys. Part 1*, Vol.40 (8), (2001) pp. 4924–4925.

[13] Li, J., Hou, L., Raun, H., Xie, Q., Gan, F., *Proc. SPIE Int. Soc. Opt. Eng*., Vol. 4085, (2001) pp. 125.

[14] Wagner, T., Frumar, M., Kasap, S.O., Vlcek, Mir., Vlcek, Mil., *J. Optoelectron. Adv. Mater.*, Vol.3 (2), (2001) pp. 227.

[15] Gutwirth, J., Wagner, T., Kohoutek, T., Vlcek, Mir., Schroeter, S., Kovanda, V., Vlcek, Mil., Frumar, M., *J. Optoelectron. Adv. Mater*., Vol. 5 (5), (2003) pp.1139.

[16] Tanaka, K., *J. Non-Cryst. Solids*, Vol.164–166, (1993) pp.1179.

[17] Wagner, T., Jilkova, R., Frumar, M., Vicek, M., *Int. J. Electron*., Vol.77, (1994) pp.185.

[18] Tanaka, K., Itoh, M., Yoshida, N., Ohto, M., *J. Appl. Phys*., Vol.78, (1995) pp. 3895.

[19] Kawaguchi, T., Maruno, S., Elliott, S.R., J. Appl. Phys., Vol.79, (1996) pp.9096.

[20] Ohto, M., *Phys. Status Solidi A*, Vol.159, (1997) pp.461.

[21] Wagner, T., Frumar, M., Suskova, V., *J. Non-Cryst. Solids*, Vol.128, (1991) pp.197.

[22] Frumar, M., Polak, Z., Cernosek, Z., Frumarova, B., Wagner, T., *Chem. Paper*, Vol.57, (1997) pp. 310.

[23] Wagner, T., J. Optoelectron. Adv. Mater., Vol.4 (3), (2002) pp.717.

[24] Ramesh, K., Asokan, S., Sangunni, K.S., Gopal, E.S.R., *J. Phys. Chem. Solids*, Vol. 61, (2000) pp. 95.

[25] Frumar, M., Cernosek, Z., Jedelsky, J., Frumarova, B., wagner, T., *J. Optoelectron. Adv. Mater.*, Vol.3 (2), (2001) pp.177.

[26] Tanaka, K., *J. Non-Cryst. Solids*, Vol.164–166, (1993) pp.1179.

[27] Wagner, T., Jilkova, R., Frumar, M., Vicek, M., *Int. J. Electron*., Vol.77, (1994) pp.185.

[28] Tanaka, K., Itoh, M., Yoshida, N., Ohto, M., *J. Appl. Phys*., Vol.78, (1995) pp. 3895.

[29] Kasap, S. O. and Juhaz, C., *J. Mater. Sci.,* Vol.24, (1986) pp.1329.

[30] Larmagnac , J. P., Grenet, J. and Michon, P., *J. Non-Cryst. Solids*, Vol.45, (1981) pp.157.

[31] Moynihan, C. T., Easteal, A. J., Wilder, J. and Tucker, J., *J. Phys. Chem.*, Vol.78, (1974) pp.267.

[32] Colemenero, J., Barandiaran, J. M., *J. Non-Cryst. Solids*, Vol. 30, (1978) pp.263.

[33] Kasap, S. O., Yannacopoulos, S., *Phys. Chem. Glasses*, Vol.31, (1990) pp. 71.

[34] Mehta, N., Tiwari, R.S., Kumar, A., *Mater. Res. Bull*., Vol.41, (2006) pp.1664.

[35] Kissinger, H. E., *Anal. Chem.*, Vol.29, (1997) pp.1702.

[36] Matusita, K., Sakka, S., *Phys. Chem. Glasses* , Vol.20, (1979) pp.81.

[37] Matusita, K., Sakka, S., *Bull Inst. Chem. Res. Kyoto Univ.*, Vol.59, (1981) pp.159.

[38] Augis, J.A., Bennett, J.E., *J. Them. Anal.*, Vol.13, (1978) pp.283.

_____

Cooke Optics receives Oscar for
"defining the look of motion pictures over the last century"

Jonathan Maxwell

The "Cooke Look" is a part of our lives, appearing every day on big screens and televisions, thanks to the company's innovative designs.

The Cooke name has been associated with cinematography since the very earliest days of the cinema -- in fact it is difficult to think of any other lens company with such a comprehensive involvement. From a very early period, the company established strategic collaborations with key players: George Eastman and then the Kodak company (from the 1890s through to the present day), Bell & Howell (the first newsreel zoom lens in 1931), Technicolor (custom color-separation lenses, from the early 1930s to the 1960s), and The Rank Organisation (zoom lenses, initially for TV and then film, from the 1950s to the 1990s). In this way the company became, from quite early on, a close family member within the cinema industry.

Principal patents and inventions have included the ground-breaking Cooke Triplet anastigmat (1893); The very first (chemical) anti-reflection coatings (1904); The Kinic cinematographic lens before World War I; The Opic and Speed Panchro lenses introduced in the 1920s (whose f/2 speed enabled the introduction of the talkies); The Cooke Varo zoom lens in 1931, and many ground-breaking Zoom lens patents in the post-World War II era.

In the 21st century, the Cooke Optics company has designed and developed three ranges of prime lenses (S4/i,T2 5/i,T1.4 and the miniS4/i,T2.8) which have spearheaded and set the international standard for electronic lens data systems. They have also introduced the T2 CXX zoom lens that has been added to the existing stable of the Cooke Varotal and Cinetal zoom lenses.

The Cooke Optics Ltd Design and Engineering headquarters are in Leicester in the UK, where 85 employees create and manufacture innovative cinematographic and stills lenses. The design procedures and adjustment techniques developed by the company have led to an enviable cinematographic reputation for what has become known as the "Cooke Look." This revered "look" is a sympathetic color depth in the images, combined with an adjusted coincidence between the sharpest image and the optimum chromatic focus.

Current and recent movies made with Cooke lenses include After Earth, A Good Day to Die Hard, Arbitrage, Harry Potter and the Half Blood Prince, To Rome With Love, and Hugo. Popular television shows include Downton Abbey, Grey's Anatomy, and Community.

The current challenges for the designers of cinematographic optics in the current era are about meeting well-established requirements, such as high apertures (for shallow depth of field rather than photographic "speed"), wide angular fields of view with low distortion in asymmetric lens constructions, low breathing (change of image scale with focusing), and extracting as much performance out of the relatively mature design and manufacturing technologies at our disposal: software, tolerancing techniques, optical glass choices, aspheric surfaces, high-speed polishing, high-efficiency wide-spectral-band anti-reflection coatings, and appropriate and efficient quality-control and optical-testing methods. All of these are active areas of development in Cooke Optics at this time.

Jonathan Maxwell is a lens designer and consultant who has worked with Cooke and Taylor Hobson over the years, and taught courses for SPIE in Europe and the United States. He has published two books on optical design.

Studying of Reflected Light Optical Laser Microscope Images Using Image Processing Algorithm

Fatema H. Rajab

Department of Laser and Optoelectronic Engineering, College of Engineering, Al-Nahrain University, Baghdad, IRAQ

In this work, the mechanism and principle of optical laser microscope (OLM) which works on the principle of light reflection that used in many applications were presented. Image of silicon wafer that obtained from OLM was enhanced and analyzed using image processing algorithm. The used algorithm was designed using MATLAB 10.0. The output images from RLOLM were compared with images of ordinary microscope.

1. Introduction

A microscope is an instrument designed to make fine details visible. Transmitted light microscope reflected light microscope, reflected/transmitted light microscope are main types of optical microscope [1]. Reflected light microscopy shown in Figure (1) is often referred to as incident light, epi-illumination, or metallurgical microscopy, and is the method of choice for fluorescence and for imaging specimens that remain opaque even when ground to a thickness of 30 microns [2]. The range of specimens falling into this category is enormous semiconductors (unprocessed silicon, wafers, and integrated circuits), slag, coal, plastics, paint, paper, wood, leather, glass inclusions and a wide variety of specialized materials. Because light is unable to pass through these specimens, it must be directed onto the surface and eventually returned to the microscopy objective by either specular or diffused reflection . Today, many microscopes manufactures offer models that permit the user to alternate or simultaneously conduct investigations using vertical and transmitted illumination .Reflected light microscopy is frequently the domain of industrial microscopy, especially in the rapidly growing semiconductor area and thus represents a most important segment of microscopically studies [3].

2. Experimental Setup

In this work, the OLM is reconstructed from ordinary reflected light microscope that shown in Figure (1) by replacing a light source with He-Ne laser (632.8nm, 4mW) as shown in Figure (2) .

The Laser light enters the objective lens of a microscope through a pinhole. An image of the pinhole is focused on the plane of the object. The beam impinging on the object is reflected from it, and an image of the illuminated spot on the object is focused on the pinhole. The light passes through the objective lens to a digital CCD camera. The outputs from a digital camera became maximum when the object is located at the focus of the lens. The image is transferred and display on computer system by

using the USB interfacing method. Scheme of work setup are shown in Figure (3).
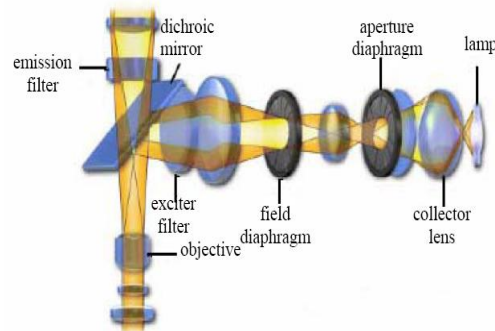
Fig. (1) Type of reflected light microscopy [3]

Fig. (2) Reflected Light Optical Laser Microscope
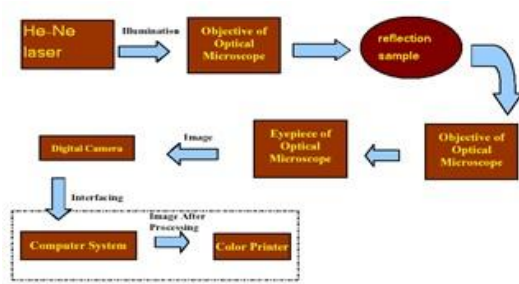
Fig. (3) Architecture of the proposed system

Optical magnification is achieved when it matches the resolution of the microscope system to the resolution of the imaging device (e.g. eye or CCD camera) [4]. The objective, which provides the resolution and most of the specimen in primary image plan. This image is viewed with an eyepiece which further magnifies and produces a virtual image for observation [5]. Combining the magnification of the objective with that of the eyepiece we obtain the total magnification of the system which may be written as [5]:

M=Mob x Mep

where Mob of microscope are 5x, 10x, 20x, 50x, 100x.

Figures (4-7) shows some examples of slides image that result using the OLM.
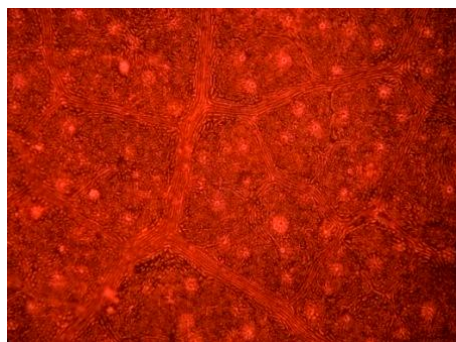
(a)
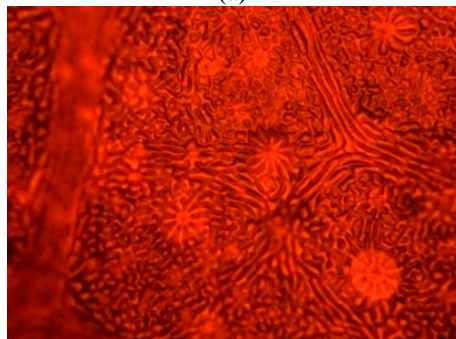
(b)
Fig. (4) Image of plant cell: (a) with 100x, (b) with 200x
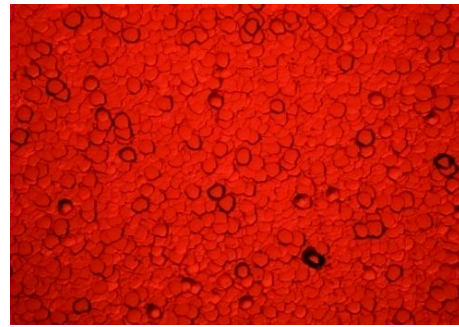
(a)
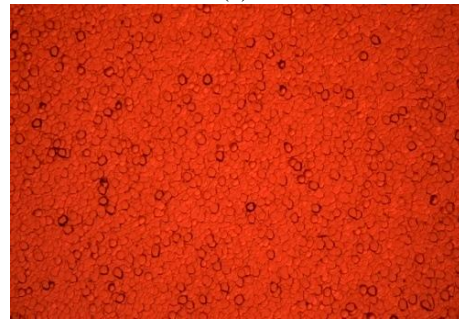
(b)
Fig. (5) Image of silicon wafer: (a) with 200x, (b) with 100x
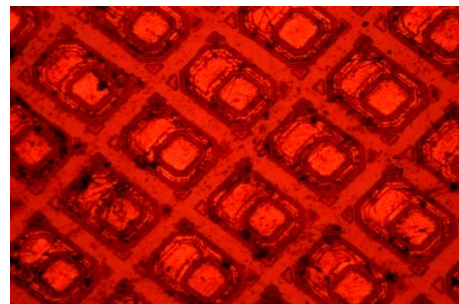
Fig. (6) Image of Integrated circuit with 100x
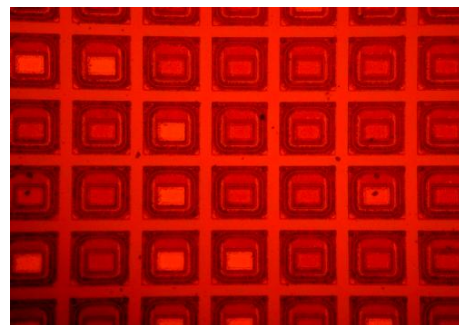
Fig. (7) Image of another Integrated circuit with 200x

Figure (8) shows some examples of slides image that result using same microscope using ordinary light.

(a)

(b)

(c)
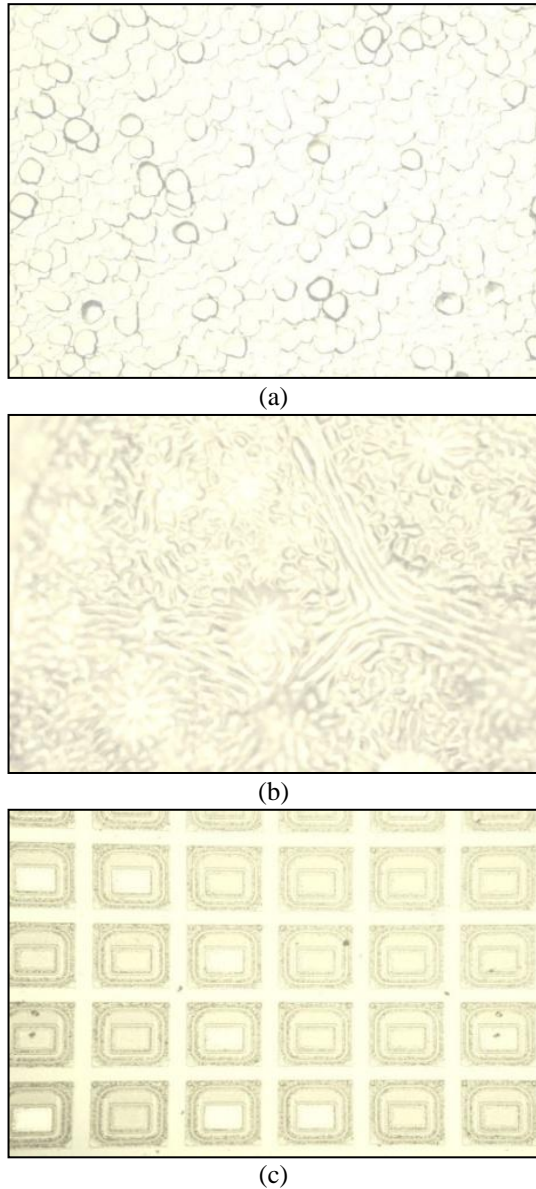
Fig. (8): (a) Image of silicon wafer with 200x (b) Image of plant cell with 200x, (c) Image of Integrated circuit slide with 200x

Using laser as the imaging light source produced images of exceptional clarity and contrast .The important characteristic of the optical laser microscope, which distinguishes it from the conventional light microscope, is that the image formation is contrast [6].

Microscope image processing algorithm is abroad term that covers the use of digital image processing technique to process, analyze, and present image obtained from OLM. The image processing algorithm that was applied to the OLM image is shown in Figure (9).
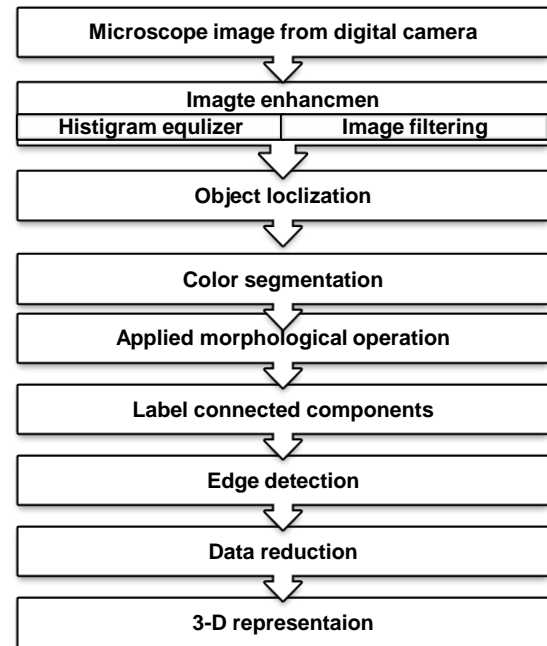
Fig. (9) Processing algorithm and 3D representation of image

3. Results and Discussion

The slides shown in Figures (10) through (21) illustrate the use of all processes of the block diagram in Figure (9) to the detection of boundaries in a microscope image of silicon wafer and presented in 2-D and 3 -D projections for the same image. Two enhancement algorithms were applied on the image of silicon wafer after converting RGB image to gray level, histogram equalization and median filtering. Figure (11) shows the image after adjustment that was achieved by redistributing the intensity along the pixel of image and the effect of Median filter on object to improve the image.
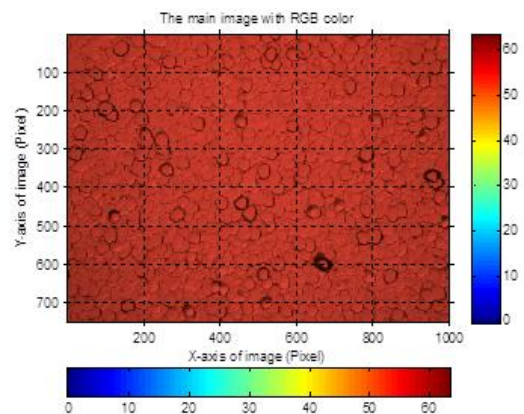
Fig. (10) Main image from RLOLM
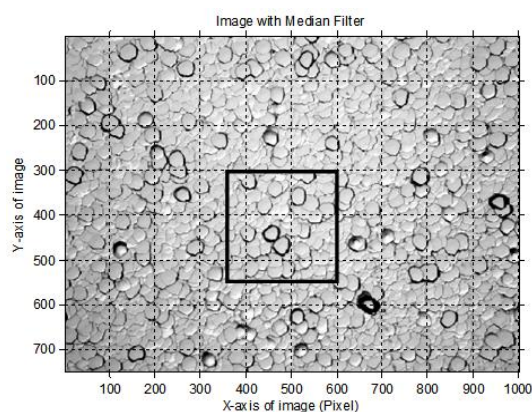
Fig. (11) Image with median filter

Fig. (13) Image after applying morphological operation

Figure (12) result after selecting an area of interest in a filtering image and display it in another window, there by magnify the area. After enhancement process and ROI are applied, the morphological operations are applied (opining, closing, eroded, reconstructions) to segment the color and labeling the objects, labeling definition is used to label different objects in the binary result. The objects are displayed with different colors from a jet color map as shown in Figure (13).

Fig. (12) ROI image

Fig. (14) Image with Canny edge detection

There are many edge detection algorithms are applied on image to find the edge of objects, canny edge detection is a best algorithm applied to ROI as shown in figure (14) to find the edge and perimeter of object. Figure (15) shows the contour display calculated from the RLOLM data. Figure (16) shows the different pixel gray values in the original image. For this type of display, the user controls over the image orientation, the eye positions, the "lighting" position and intensity, and surface reflection characteristics.

Fig. (15) Contour display of the OLM data file with 8 contour levels
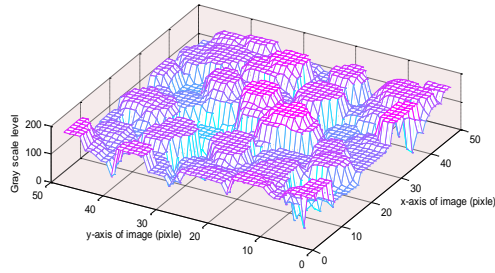
Fig. (16) Gray level relief of the silicon wafer surface of figure (12)

4. Conclusions

RLOLM is a quantitative device for study of semiconductor materials and devices, and biological specimens including living cells. RLOLM images are clearly, most contrast as compared with ordinary light microscope images. Image processing algorithm that used for analyze and study the silicon wafer is suitable algorithm for any semiconductor material or device specially for finding the edges of objects.

References

[1] Mortimer A., "Microscope: Basics and Beyond", Olympus America, Inc., *vol.*1, (2003).

[2] Bradbury S., "An Introduction to the Optical Microscope", revised Edition by Oxford University press, New York, (1995).

[3] Cell Biology: Microscopy Labs, "Introduction to Fluorescence Microscopy", Kent State University.

[4] Julio V., "Microscopy Tutorial", Scientific Imaging Shared Resource Fred Hutchinson Cancer Research Center, (2003).

[5] Bradbury S.," An Introduction to the Optical Microscope", revised Edition by Oxford University Press, New York, (1995).

[6] Diaspro A., Sartore M., and Nicolini C.," 3D Representation of Bio- Structures Imaged with an Optical Microscope", Image and vision computing, *vol.* 8, *No.* 2, (1990).

First announcement and call for papers

Plasmas, Surfaces and Thin Films

12 June 2013
Institute of Physics, 76 Portland Place, London W1N 4AA

Organised by the IOP Ion and Plasma Surface Interactions Group (IPSI)
Co-sponsored by the IOP Vacuum Group and the Thin Films and Surfaces Group

www.iop.org/conferences

Introduction

This one day meeting has become an annual event providing a forum for those involved in using plasmas or ion beams for surface modification and thin film deposition. Topics covered include modelling of fundamental aspects of plasmas and their interaction with surfaces through to new techniques for high throughput industrial processes. The meeting usually attracts equal numbers of participants from universities and industry.

The meeting will start at 10:00 with registration and refreshments. The programme will commence at 10:30 and finish at 17:00. The programme will be available on the website in May 2013.

Organisers

Prof. Roger Smith, Loughborough University (**R.Smith@lboro.ac.uk**)
Prof. Mike Walls, Loughborough University (**J.M.Walls@lboro.ac.uk**)

Speakers confirmed

- **Atmospheric pressure plasma jets: Dynamics and opportunities for surface engineering**
  James Walsh (Liverpool University)
- **Nanometric coating on glass: from Low-e to triple silver coatings**
  Raf Dressen (AGC Glass Europe)
- **The current status in modelling reactive magnetron sputtering**
  Diederik Depla (Ghent University)
- **Sputter deposition of solid electrolytes and mixed conductors for energy and environment applications**
  Alain Billard (Université de Technologie de Belfort-Montbéliard)
- **The deposition of thin films using HiTUS**
  Steve Wakeham (Plasma Quest)

Further 10 minute contributions and a limited number of poster presentations are invited. Abstracts should be submitted via the conference web site – **www.iop.org/conferences** – by Friday 26 April 2013.

Please also send a title of your abstract by e-mail to; Professor Roger Smith,Loughborough University (**R.Smith@lboro.ac.uk**)

Enquiries

Dawn Stewart
The Institute of Physics, 76 Portland Place, London W1B 1NT
E-mail: **dawn.stewart@iop.org**
Tel +44 (0)20 7470 4800
Fax +44 (0)20 7470 4848

IOP | Institute of Physics
Ion and Plasma Surface
Interactions Group

Institute of Physics, 76 Portland Place, London, W1B 1NT
Tel +44 (0) 20 7470 4800
E-mail: conferences@iop.org
www.iop.org

Lowering the Threshold Current of Photonic Crystal Vertical-Cavity Surface-Emitting Lasers

Yi-Yang Xie, Chen Xu
Key Laboratory of Optoelectronics Technology
Ministry of Education
Beijing University of Technology
Beijing, China

Qiang Kan, Chun-Xia Wang, Hong-Da Chen
State Key Laboratory of Integrated Optoelectronics
Institute of Semiconductors
Chinese Academy of Sciences
Beijing, China

Chen Xu
Key Laboratory of Optoelectronics Technology
Ministry of Education
Beijing University of Technology
Beijing, China

Reducing the oxide aperture diameter to match the central defect region leads to high single-fundamental-mode output devices.
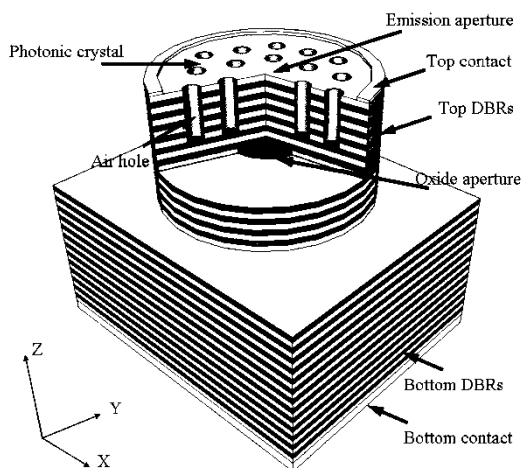
Figure 1. *Schematic 3D view of the photonic crystal vertical-cavity surface-emitting laser (PhC-VCSEL) containing 22.5 pairs of p-type top distributed Bragg reflectors (DBRs) and 34.5 pairs of n-type bottom DBRs. Both consist of aluminum gallium arsenide ($Al_{0.9}Ga_{0.1}As$ and $Al_{0.12}Ga_{0.88}As$, except for a 30nm $Al_{0.98}Ga_{0.02}As$ oxidation layer inserted in the base of the DBRs.)*

The oxide aperture reduces modal discrimination, finally deteriorating single-mode operation. However, as the oxide aperture diameter increases, the high-order mode losses quickly increase because of scattering from photonic crystal air holes, while the fundamental mode loss remains low: see Figure 2(c and d). The oxide aperture needs to be much larger than the emission aperture to be able to isolate the photonic-crystal-induced index changes from those of the oxidized layer, because the optical confinement is provided mainly by the photonic crystal structure. While the oxide aperture provides only the electrical confinement, the photonic crystal structure can confine the

In recent years, photonic crystal vertical-cavity surface-emitting lasers (PhC-VCSELs) have attracted significant attention. Characteristics such as single-mode operation in a large cavity area (which results in high single-mode output power),[1,2] high-speed modulation,[3] and a small circular divergence angle of the output beam profile[4] make them suitable for optical communications and sensing applications. In addition, they are easy to design and fabricate,[5] and polarization-stable devices with single fundamental-mode operation have been fabricated.[6] However, the abnormally high PhC-VCSEL threshold current has puzzled researchers. Reducing the threshold current is necessary to reduce power consumption and thermal losses, and improve the PhC-VCSEL devices' stability and reliability.

We used theory and experiment to optimize the relation between the oxide aperture and light emission aperture of the PhC-VCSELs so that we obtained both high single-mode output and low threshold current (see Figure 1). We used the full 3D (FDTD) method to analyze the effect of the oxide aperture diameter on the optical characteristics. FDTD takes not just the oxide aperture diameter into account but the whole structure. We used cavity mode loss analysis to investigate the single-mode operation of the laser and find the minimum oxide aperture required to maintain the single-mode performance of the device with a low threshold current.

The simulation results shown in Figure 2(a and b) show that the oxide aperture diameters in an appropriate range determine the threshold current and also, for those devices with a 7μm light emission aperture diameter, affect the higher-order modes. The oxide aperture provides additional transverse confinement to the transverse mode and reduces higher modes more significantly than the light emission aperture does.

crystal to keep the PhC-VCSELs operating in single mode and with low threshold current. We obtained PhC-VCSELs with single-fundamental-mode continuous wave 3.1mW output and threshold current of 0.9mA. We are now building on these promising results by controlling the etching depth and quality to further improve PhC-VCSEL characteristics.

Figure 3. (a) Optimized PhC-VCSEL with 8µm oxide aperture operating in a single fundamental lateral mode with 3.1mW output power. (b) Shows spectral characteristic of the optimized single mode PhC-VCSEL at maximum output power. Side suppression of more than 35dB is maintained through rollover.
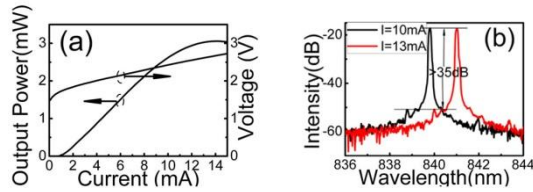
References:

1. D. S. Song, S. H. Kim, H. G. Park, C. K. Kim, Y. H. Lee, Single-fundamental-mode photonic-crystal vertical-cavity surface-emitting lasers,*Appl. Phys. Lett.* 80, p. 3901-3903, 2002.

2. A. J. Danner, J. J. Raftery, P. O. Leisher, K. D. Choquette, Single mode photonic crystal vertical cavity lasers, *Appl. Phys. Lett.* 88, p. 1114-1116, 2006.

3. C. Chen, P. O. Leisher, D. M. Kuchta, K. D. Choquette, High-speed modulation of index-guided implant-confined vertical-cavity surface-emitting lasers, *IEEE J. Sel. Top. Quant. Electron.* 15, p. 673-678, 2009.

4. H. P. D. Yang, I. C. Hsu, F. I. Lai, G. Lin, R. S. Hsiao, N. A. Maleev, S. A. Blokhin, H. C. Kuo, J. Y. Chi, Beam profile characteristics of InGaAs sub-monolayer quantum-dot photonic-crystal VCSELs, *Opt. Comm.* 274, p. 94-99, 2007.

5. N. Yokouchi, A. J. Danner, K. D. Choquette, Two-dimensional photonic crystal confined vertical-cavity surface-emitting lasers, *IEEE J. Sel. Top. Quant. Electron.* 9, p. 1439-1445, 2003.

6. D. S. Song, Y. J. Lee, H. W. Choi, Y. H. Lee, Polarization-controlled, single-transverse-mode, photonic-crystal, vertical-cavity, surface-emitting lasers, *Appl. Phys. Lett.* 82, p. 19 3182-3184, 2003.

7. Y. Y. Xie, Q. Kan, C. Xu, Y. X. Zhu, C. X. Wang, H. D. Chen, Low threshold current single fundamental mode photonic crystal VCSELs,*IEEE Photon. Technol. Lett.* 24(6), p. 464-466, 2012.

8. Y. Y. Xie, C. Xu, Q. Kan, C. X. Wang, H. D. Chen, G. D. Shen, High power single mode output low threshold current photonic crystal vertical cavity surface emitting lasers, *Proc. Optical Fiber Comm. Conf.* , p. OW1G.3, 2012.

fundamental mode, dissipate the high mode, and operate the device in single mode.[7,8]
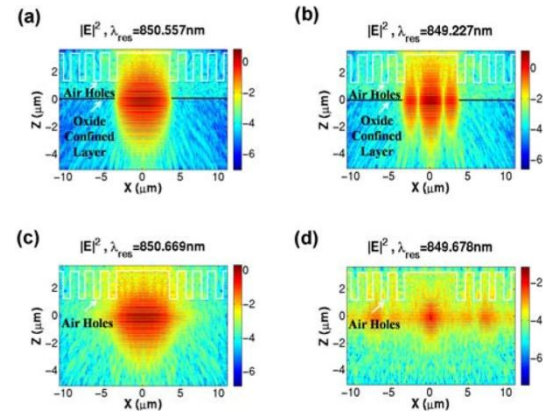
Figure 2. Mode intensity profiles in logarithmic color scale for comparison of PhC-VCSELs with different oxide aperture diameters. (a) and (b): 7µm oxide aperture diameter with fundamental and higher-order mode intensities, respectively. (c) and (d): 20µm oxide aperture diameter with fundamental and higher-order mode intensities, respectively. White lines indicate the air hole contours of the photonic crystal. Black lines indicate the oxide aperture's contours. $|E|^2$: Mode intensity of cavity. λ_{res}: Resonant wavelength of the cavity. X, Z: Co-ordinates as defined in Figure 1.

Experiments show the power-current/current-voltage and far-field distribution characteristics of our fabricated PhC-VCSEL: see Figure 3(a). The maximum output power is 3.1mW at a record low-threshold current of 0.9mA. The slope efficiency and differential series resistance of the device are 0.247W/A and 57.23Ω, respectively: see Figure 3(b), which demonstrates the optical spectrum of the PhC-VCSEL. We can see that the full width at half maximum of the device is less than 0.1nm (restricted by the resolution of the optical spectrum analyzer), and the side-mode suppression ratio is 35dB, at maximum power. The vertical and horizontal direction divergence angles are less than 10° and one intensity peak, illustrating that we improved beam quality by introducing the photonic crystal on the top DBRs.[7]

In conclusion, we demonstrated, both theoretically and experimentally, a useful and reliable way to reduce the threshold current of PhC-VCSELs by reducing the oxide aperture and optimally matching it with the emission aperture. The oxide aperture should be larger than the emission aperture of the photonic crystal structure by one air hole diameter (1µm) of the photonic

Effect of Heat Treatment on the Optical Properties of ZnO Thin Films Prepared by Chemical Spray Method

Ghazi Y. Nasser

Department of Physics, College of Education, Al-Iraqia University, Baghdad, IRAQ

ZnO is one of transparent conducting oxide materials whose thin films attract much interest because of typical properties such as high chemical and mechanical stability in hydrogen plasma, high optical transparency in the visible and near-infrared region. Due to these properties ZnO is a promising material for electronic or optoelectronic application such as solar cells (anti-reflecting coating and transparent conducting materials), gas sensors, liquid crystal displays, heat mirrors, surface acoustic wave and bulk acoustic devices (piezoelectric devices), multilayer photo- thermal conversion systems, etc.

In this research, thin films of ZnO of thickness 5200Å±30 prepared using chemical spray method. The films deposited on Crown glass substrates Optical studies show that in these films the electronic transition is of the direct transition type. The optical energy gap for the films of as deposited and for those heat treated for an hour at different temperatures is estimated to be in the range 3.05-3.2 eV. Results analysis exhibits the dependence of optical energy gap on the temperature of heat treatment.

1. Introduction

In the last decade, Zinc Oxide (ZnO) thin film attracts much interest due to valuable properties such as it is high resistance to chemical attack, chemical stability and good adherence to many substrates. High optical transparent in the visible region and the index of refractive is ~1.8 enables them to act as a antireflection coating in solar cells applications. Also, its abundant in nature makes it a lower cost material when compared with ITO and SnO_2 materials.

Zinc oxide (ZnO) is a widely used functional material with wide and direct band gap, large exciton binding energy, and excellent chemical and thermal stability. ZnO is a semi-conducting material widely used as transparent electrodes in solar cells, chemical and gas sensors, spintronic devices, and light emitting diodes. Nowadays, the sol-gel method has been extensively used to obtain various kinds of functional oxide films due to its simplicity and low cost. It has been found that post-annealing plays an important role on the properties of ZnO films, and the optical transmittance and photoluminescence are very sensitive to the quality of crystal structure and to the presence of defects.

Also, ZnO is one of transparent conducting oxide materials whose thin films attract much interest because of typical properties such as high chemical and mechanical stability in hydrogen plasma, high optical transparency in the visible and near-infrared region [1-3]. Due to these properties ZnO is a promising material for electronic or optoelectronic application such as solar cells (anti-reflecting coating and transparent conducting materials), gas sensors, liquid crystal displays, heat mirrors, surface acoustic wave and bulk acoustic devices (piezoelectric devices), multilayer photo- thermal conversion systems, etc [4-8].

Thin films of ZnO have been prepared by using several deposition techniques which include chemical vapor deposition, RF/DC magnetron sputtering, oxidation of evaporated metallic film, spray pyrolysis, pulsed laser deposition, sol- gel technique, etc [9-13]. Among these methods, the spray pyrolysis technique has several advantages such as simplicity, safety, and low cost of the equipments and raw materials. With the spray process, the solution is sprayed directly onto the substrate by means of a nozzle assisted by a carrier gas. When the fine droplets arrive at the substrate, the solid compounds react to become a new chemical compound. The quality and physical properties of the films depend on the various process parameters, such as substrate temperature, molar concentration of the starting solution, spray rate, pressure of the carrier gas and the geometric characteristics of the spray system.

In this research work, we report a study on optical properties of, ZnO thin films prepared by spray pyrolysis technique.

2. Experiment

ZnO films were prepared on crown glass substrates by spray pyrolysis technique. The spray

solution used was of 0.2M of high purity zinc acetate dehydrate $Zn(CH_3COO)_2.2H_2O$, isopropyl alcohol and distilled water (Volume ratio 3 to 1). The solution was stirred at 300K for 1 hour by a magnetic stirrer to get a clear homogeneous solution. The atomization of the solution into a spray of fine droplets was carried out by the nozzle, with the help of compresses air as carrier gas. The flow rate of solution was 8 ml/min and the substrate temperature was held constant at 473K using a chromel-alumel thermocouple with the help of a digital multimeter supplied by Pasco. The nozzle to substrate distance was 50 cm and the diameter of nozzle was 0.3 mm.

The substrates were cleaned by acetone, alcohol and finally with distilled water before coating. Each coated substrate was dried at 473K for 10 min to evaporate the solvent and remove the organic residuals. The process repeated many times to obtain the desired thickness. The heat-treated films placed into evacuated tube furnace and annealed under law pressure of 10^{-1} torr using a mechanical rotary pump for 1 hour.

Film thickness determined by the weight–difference method ($d=M/\rho A$, where A is the area of the film, M its mass, d its thickness and ρ its density, 5.61 g/cm^3) using an electronic precision balance. The optical transmission and absorbance of the films were obtained in the Ultraviolet/visible/near infrared region up to 1100 nm using 800 Philips double beam spectrophotometer.

3. Results and Discussion

Figure (1) shows the optical transmission spectra of ZnO thin films of thickness 5200Å±30 for as deposited sample S3 (RT) and heat treated samples S2 (423 K) and S1 (523 K).
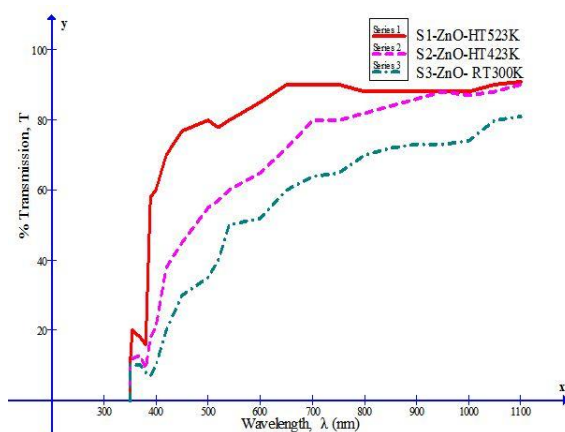
Fig. (1) Transmission spectra of the sprayed ZnO thin films of as deposited and heat treated samples

These spectra show that for film S1 which heat-treated at 523 for 1 hour, the average transmission over the range 500-1100 nm exceeds 80% with a sharp fall near the fundamental absorption; whereas

fall in transmission is gradual for the sample S2 which heat treated at 423 K for 1 hour and for the sample S3 which is left at room temperature (300 K).

It is clear from Fig. (2) for the absorption spectra that the films have low absorbance in the visible/infrared region while absorbance is high in the ultraviolet region. The absorption coefficient (α) was calculated using Lambert law as follow [14].

$$\alpha = \frac{2.303\,A}{d} \qquad (1)$$

where, d is the thickness of the films, and A is the optical absorbance
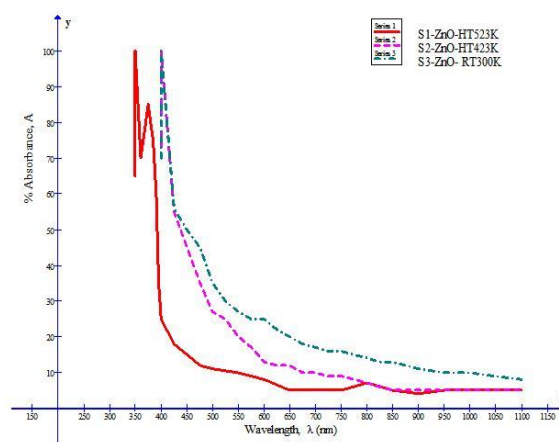
Fig. (2) Transmission spectra of the sprayed ZnO thin films of as deposited and heat treated samples

These absorption coefficients values were used to determine optical energy gap. Figure (3) shows the plot of $(\alpha h\nu)^2$ vs. $h\nu$, where $h\nu$ is the energy of the incident photon. The energy gap was estimated by assuming a direct transition between valence and conduction bands from the expression:

$$\alpha h\nu = K\left(h\nu - E_g\right)^{\frac{1}{2}} \qquad (2)$$

where K is a constant, E_g is determined by extrapolating the straight line portion of the spectrum to $\alpha h\nu=0$

From this graph, the optical energy of as deposited sample S3 (300 K) is 3.05 eV, the optical energy gap of heat treated sample S2 (423K) is 3.08 eV and the optical energy gap of heat treated sample S1 (523K) is 3.2 eV. These values are slightly smaller than the bulk value of 3.31 eV [15] and in good agreement with previously reported data of ZnO thin films [16]. The optical absorption edge has been observed at a wavelength of about 385 nm corresponding to band gap of about 3.05 eV for non-annealed sample S3.

The UV emission peak originates from excitonic recombination as shown by other researchers, and the UV peak intensity varies with annealing temperatures. Defect-related green emission is believed to come from oxygen vacancies [17]. Generally, it is thought that the quality of ZnO films improve with increasing annealing temperatures. However, it is noteworthy that the ZnO film annealed at 450°C shows strong excitonic related UV emission, and the UV emission intensity monotonically increases at annealing temperatures beyond 500°C. This behavior can be understood phenomenally by considering the formation of defects. While the ZnO film was annealed at 450°C, the rate of formation point defects, which is responsible for radiative recombination, is low at low temperature. Accordingly, efficient excitonic emission can be easily achieved. For the temperature higher than 450°C, more defects responsible for the nonradiative transition will be introduced into the films. This is why film annealed at temperatures higher than 500°C would show poor UV emission than that annealed at 450°C. Furthermore, higher annealing temperatures facilitate the migration of grain boundaries and promote the coalescence of small crystals, and thus favor a decrease of the concentration of nonradiative recombination centers [18]. Annealing at temperatures higher than 500°C may be the subject of future studies on zinc oxide thin films.

Fig. (3) Plot of $(\alpha h\nu)^2$ for sprayed ZnO thin films of as deposited and heat treated samples

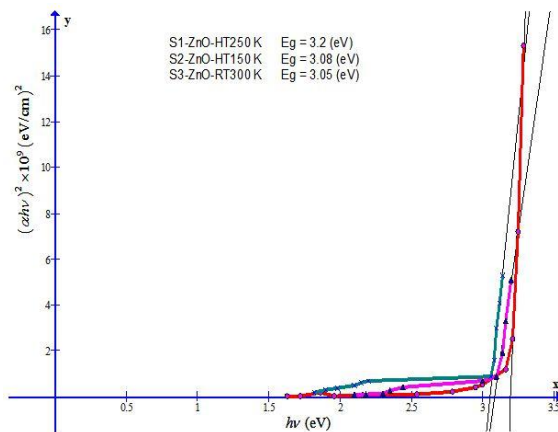The observed band gap energy of the heat treated sample S3 (523K) which is 3.2 eV correspond to a wavelength of about 370 nm, which is close to that of single crystal. These results show that the band gap energy of ZnO thin films shits to higher energy values after annealing (Fig. 4). The increase of the band gap energy after annealing is consistent with some of the following studies in the literature. For example, Bouhssira et al. have shown that the band gap energy increases from 3.3 eV in as grown up to

3.7 eV after systematic annealing experiment at temperatures from 373 K to 873 K [19]. Xue et al. has observed almost no change, a little 10 meV increase in the band gap energy up to 1023 K annealing temperature and a decrease of about 10 meV at annealing temperatures between 1023-1223 K [20]. They attribute the blue shift of the optical absorption edge to the increasing crystallinity of the ZnO films. Furthermore Zou et al. showed the increase in the band gap energy from 3.18 eV to 3.2 eV after annealing as well [21].

The increase in transmittance with higher annealed temperature may be due to deceasing optical scattering caused by the densification of grains followed by grain growth and the reduction of grain boundary density [22].
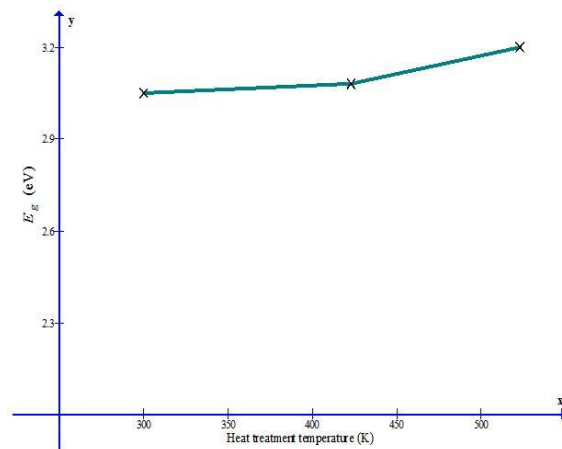
Fig. (4) Optical energy gap vs. heat treatment of the ZnO films

The smaller E_g values attributed to O content on the surface of the films [22]. We think that most annealing treatments cause evaporation of oxygen and the sample become more Zn-rich. Since the O-rich samples usually have lower band gap energy, relatively more Zn-rich samples after annealing due to the evaporation of excess oxygen from the surface will have higher band gap energies in comparison to the as deposited samples.

4. Conclusion

ZnO thin films of as deposited and heat treated at different temperatures prepared by spray pyrolysis technique have been studied for their optical properties. Analysis of UV/VIS spectra of the films reveals that the materials to be of direct electronic transition with an energy gap in the range 3.05 to 3.2eV. The optical characterization on both as deposited and heat treated samples have shown that the heat treatment carried out at 523K has a great influence on the optical energy gap. It has been observed that the direct band gap was increased from 3.05 eV for as deposited sample to 3.2 eV after

annealing at 523K for 1 hour. We think that this increase in band gap energy may be due to the low oxygen content of the sample surface after heat treatment.

References

[1]   P. Nunes et al., *Thin Solid Films*, 337, 176 (1999).

[2]   D.J. Goyal et al., *J. Mater. Sci.*, 27, 4705 (1992).

[3]   A. Sanchez- Juarez, A. Tiburcio- Silver and A. Ortiz, *Sol. Energy Mater. Sol. Cells*, 52, 301 (1998).

[4]   L. Chopra, S. Major and D.K. Panday, *Thin Solid Films*, 1021, 1 (1983)

[5]   S. Bose and A.K. Barua, *J. Phys. D: Appl. Phys.*, 32, 213 (1999).

[6]   H. Kim and C.M. Gilmore, *Appl. Phys. Lett.*, 76, 259 (2000).

[7]   T. Yamamoto, T. Shiosaki and A. Kawabata, *J. Appl. Phys.*, 51, 3113 (1980).

[8]   H. Kim, *J. Korean Phys. Soc.*, 32, S1741 (1988).

[9]   F. Chaabouni, M. Abaab and B. Rezig, *Mater. Sci. Eng.*, B109, 236 (2004).

[10] Y. Natsume and H. Sakata, *Thin Solid Films*, 372, 30 (2000).

[11] M. Jin et al., *J. Vac. Sci. Technol.*, A13, 92 (2006).

[12] V. Muast et al., *Thin Solid Films*, 502, 219 (2006).

[13] D.W. Lane et al., *Thin Solid Films*, 221, 262 (1992).

[14] A. Adachi, A. Kudo and T. Sakata, *Bull. Chem. Surf. Technol.*, 155, 141(2002).

[15] S. Oktik, *Prog. Cryst. Growth Charact.*, 17, 171(1988).

[16] F. Paraguay et al., *Thin Solid Films*, 350, 192(1999).

[17] N. Bouhssira et al., *Appl. Surf. Sci.*, 252, 5594 (2006).

[18] S.W. Xue et al., *J. Alloy Comp.*, 423, 265(2007).

[19] H.S. Kang et al., *Mater. Sci. Eng.*, B102, 313 (2003).

[20] W.C. Chen et al., Proc. of E-MRS Symp., 2005, Strasburg (France), Superlattices and Microstructures.

[21] Zou et al., *Mater. Lett.*, 61, 4305 (2007).

[22] H. Li et al., *Vacuum*, 77, 57 (2004).

[23] R. Hong et al., *J. Cryst. Growth*, 284, 347 (2005).

_____

Quantum Microcavities as Efficient Radiation Sources

Mikhail Glazov
Senior Scientific Researcher
Ioffe Physical Technical Institute
Russian Academy of Sciences and
State University of St. Petersburg,
St. Petersburg, Russia

A semiconductor microcavity consisting of a quantum well sandwiched between two mirrors may produce laser light with specific frequency, coherence, and polarization.

A laser is a radiation-emitting device that typically works through the stimulated emission of photons and has uses in fields from fundamental research to medicine and the military. One of the most important parameters of a laser is its threshold, the value of input power or current above which laser generation takes place, i.e., the radiation becomes coherent. The working principle of quantum-microcavity lasers, where the light is emitted spontaneously, is different from that of conventional devices: they are based on the stimulated scattering of radiation rather than on stimulated emission, which makes it possible to reduce the laser threshold dramatically.
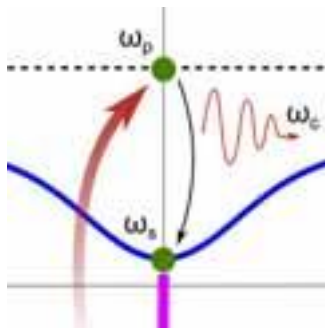
A quantum microcavity is a microstructure where an active (light-emitting) layer, usually a quantum well, is placed between two mirrors. This enables a strong light-matter coupling where energy is coherently transferred back and forth between a photon trapped in the cavity and an exciton (electron-hole pair), the elementary excitation of the material: see Figure [1]. This strong coupling, first observed in 1992,[1] results in the formation of novel half-light half-matter quasiparticles known as exciton-polaritons, which many researchers have studied in the past two decades.[2,3]

The fact that exciton-polaritons can condense to form a macroscopically coherent state opens up the possibility of creating a polariton laser with small emission threshold and extended temporal and spatial coherence of radiation.[4] The stimulated scattering of polaritons toward the ground state, which enhances the radiation of the microcavity, is created non-resonantly by optical or electronic pumping. The energy of the optical transition in the active layer determines the lasing energy. For gallium-nitride-based structures it amounts to about 3.4eV corresponding to the violet end of the visible spectrum. Structures based on cadmium telluride emit at about 1.7eV—i.e., red light—and gallium-arsenide-microcavity radiation reaches the near-IR spectral range. The choice of proper material makes it

possible to address a specific spectral part, while the fine tuning of emission energy can be realized by structure design and external factors: electric or magnetic fields, mechanical strain, and so forth. In our work, we theoretically studied the fundamental properties of quantum-microcavity lasers, namely, their coherence and polarization.
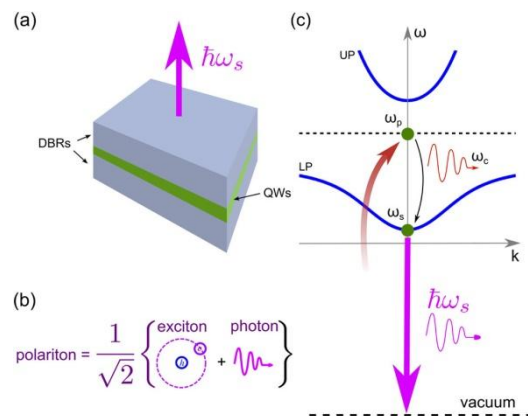
Fig. (1) *(a) The structure considered in this work: a semiconductor microcavity consisting of an active layer containing quantum wells (QWs) sandwiched between two distributed Bragg reflectors (DBRs). (b) Illustrative scheme of the exciton-polariton as a coherent superposition of an exciton (electron-hole pair) and a photon. (c) Schematic of the polariton dispersion relation, showing the lower-polariton (LP) and upper-polariton (UP) branches. The emission of visible radiation with frequency $\hbar\omega_s$ is shown. The excited 2p exciton state with frequency ω_p and terahertz transition with frequency ω_c are also illustrated. k is the wavevector of the exciton-polariton.*

The key feature of the laser light is its coherence or ability to interfere. The temporal coherence related to the linewidth and spatial coherence are distinguished. The latter parameter, called $g^{(1)}(r)$, is related to the possibility for the system to share the same wavefunction at a distance r. Experiments show that if the condensate is formed, $g^{(1)}$ enhances strongly but still drops to zero for relatively large distance r, typically larger than 10μm. The origin of this decay may be related either to the phase fluctuations of the condensate or the fluctuations of the condensate amplitude.[5–7] Our recent work, carried out together with experimentalists from the Lebedev Physical Institute and the Institute of Solid State Physics, both of the Russian Academy of Sciences, aimed to clarify this issue.[8] We demonstrated that, at least for the pulsed

excitation regime, the amplitude fluctuations are still large and limit the spatial coherence.

In addition to frequency and intensity, the radiation is characterized by its polarization, with the polarization state of the wave being directly related to the orientation of the photon spin. The condensate is usually linearly polarized due to the symmetry breaking that accompanies the condensation process. We recently predicted and observed the optical spin Hall effect, which results in the conversion of linear to circular polarization of light in a microcavity.[9,10] Of relevance for practical application, this effect can be used to generate polaritons and polariton fluxes with given spin or polarization state propagating over macroscopic distances.

As noted above, the emission of quantum microcavities usually corresponds to the visible range of the light spectrum. Our recent work suggests that such a structure can also be used to emit terahertz radiation.[11] The creation of a terahertz source is important due to various applications in modern technology such as information transfer and sensing.[12,13] The main obstacle in this field is the low rate of spontaneous emission of terahertz photons. According to Fermi's golden rule, this emission is proportional to the cube of the frequency and for terahertz transitions should be roughly tens of inverse milliseconds, while lifetimes of crystal excitations typically lie in the picosecond range. Strategies tried to improve the terahertz emission rate include using the bulky molecular or free-electron lasers,[13] the Purcell effect obtained by embedding the sample inside a terahertz cavity,[14,15] and the cascade effect in quantum-cascade lasers.[16,17]

We proposed a simpler route toward terahertz emission that uses two-photon pumping of the excited $2p$ exciton state: see Figure 1(c). This idea was inspired by other researchers who realized the two-photon pumping in gallium-arsenide-based quantum-well structures.[18] The direct transition to or from the $2p$ exciton state with emission or absorption of a single photon is forbidden by optical selection rules. Instead, a $2p$ exciton can radiatively decay to the lower exciton-polariton mode formed by the $1s$ (ground-state) exciton and cavity photon. This transition is accompanied by the emission of a terahertz photon. The terahertz transition from the $2p$ state pumps the lowest-energy exciton-polariton state, which eventually leads to polariton lasing (emission of coherent light). As a macroscopic occupation of the lowest-energy polariton state stimulates emission of terahertz photons, in the polariton lasing regime the cavity would ideally emit one terahertz photon for each optical photon emitted by the polariton laser. Our calculations show that such a situation is feasible.[11]

Quantum-microcavity systems can provide a playground for fundamental physics and may be useful for light-emitting-device applications. In our work, we suggested a way to control the polarization of quantum-microcavity emission based on the optical spin Hall effect and put forward a model of coherence propagation in exciton-polariton condensates. We anticipate that quantum microcavities can emit both visible light and terahertz radiation under specific conditions. In the future, we will theoretically model realistic devices to study the role of fluctuations in, e.g., the polarization of emission. Experiments in this area, in particular the detection of terahertz radiation from two-photon pumped quantum microcavities, are needed.

References:
1. C. Weisbuch, M. Nishioka, A. Ishikawa, Y. Arakawa, Observation of the coupled exciton-photon mode splitting in a semiconductor quantum microcavity, *Phys. Rev. Lett.* 69(23), p. 3314-3317, 1992.
2. A. Kavokin, J. Baumberg, G. Malpuech, F. Laussy, *Microcavities*, Oxford University Press, 2011.
3. D. Sanvitto and V. Timofeev (eds.), *Exciton Polaritons in Microcavities*, Springer, 2012.
4. S. Christopoulos, G. B. H. von Högersthal, A. J. D. Grundy, P. G. Lagoudakis, A. V. Kavokin, J. J. Baumberg, G. Christmann, Room-temperature polariton lasing in semiconductor microcavities, *Phys. Rev. Lett.* 98, p. 126405, 2007.
5. H. Deng, G. S. Solomon, R. Hey, K. H. Ploog, Y. Yamamoto, Spatial coherence of a polariton condensate, *Phys. Rev. Lett.* 99, p. 126403, 2007.
6. G. Nardin, K. G. Lagoudakis, M. Wouters, M. Richard, A. Baas, R. André, L. S. Dang, B. Pietka, B. Deveaud-Plédran, Dynamics of long-range ordering in an exciton-polariton condensate, *Phys. Rev. Lett.* 103, p. 256402, 2009.
7. G. Roumpos, M. Lohse, W. H. Nitsche, J. Keeling, M. H. Szymanska, P. B. Littlewood, A. Löffler, Power-law decay of the spatial correlation function in exciton-polariton condensates, *Proc. Nat'l Acad. Sci.* 109(17), p. 6467, 2012.
8. V. V. Belykh, N. N. Sibeldin, V. D. Kulakovskii, M. M. Glazov, M. A. Semina, C. Schneider, S. Hofling, M. Kamp, A. Forchel, Coherence expansion and polariton condensate formation in a semiconductor microcavity, *Phys. Rev. Lett,* 2012.
9. A. Kavokin, G. Malpuech, M. Glazov, Optical spin Hall effect, *Phys. Rev. Lett.* 95, p. 136601, 2005.
10. C. Leyder, M. Romanelli, J. P. Karr, E. Giacobino, T. C. H. Liew, M. M. Glazov, A. V. Kavokin, G. Malpuech, A. Bramati, Observation of the optical spin Hall effect, *Nat. Phys.* 3, p. 628-631, 2007.
11. A. V. Kavokin, I. A. Shelykh, T. Taylor, M. M. Glazov, Vertical cavity surface emitting terahertz laser, *Phys. Rev. Lett.* 108, p. 197401, 2012.
12. D. Dragoman, M. Dragoman, Terahertz fields and applications, *Prog. Quantum Electron.* 28(1), p. 1-66, 2004.
13. S. Ganichev, W. Prettl, *Intense Terahertz Excitation of Semiconductors*, Oxford University Press, 2006.
14. J.-M. Gerard, B. Gayral, Strong Purcell effect for InAs quantum boxes in three-dimensional solid-state microcavities, *J. Lightwave Technol.* 17(11), p. 2089-2095, 1999.
15. Y. Todorov, I. Sagnes, I. Abram, C. Minot, Purcell enhancement of spontaneous emission from quantum cascades inside mirror-grating metal cavities at THz frequencies, *Phys. Rev. Lett.* 99, p. 223603, 2007.
16. R. F. Kazarinov, R. A. Suris, Possibility of amplification of electromagnetic waves in a semiconductor with a superlattice, *Sov. Phys. Semicond.* 5, p. 707, 1971.
17. J. Faist, F. Capasso, D. L. Sivco, C. Sirtori, A. L. Hutchinson, A. Y. Cho, Quantum cascade laser, *Science* 264(5158), p. 553-556, 1994.
18. E. L. Ivchenko, *Optical Spectroscopy of Semiconductor Nanostructures*, Alpha Science International, 2005.

Wu Wei [1]
Bian Jiming [1]
Sun Yinglan [1]
Cheng Chuanhui [1]
Sun Jingchang [2]
Liang Hongwei [1]
Luo Yingmin [1]
Du Guotong [1]

Low-Temperature Aqueous Chemical Growth of Inorganic-Organic Hybrid Junction with ZnO Nanorods/Polyfluorene Structure

[1] *School of Physics and Optoelectronic Engineering, Dalian University of Technology, Dalian, 116024, China*
[2] *School of Physics and Electronic Technology, Liaoning Normal University, Dalian 116024, China*

In this paper, we report the inorganic-organic hybrid junction synthesized on ITO glass substrate, which was consisted of an n-type ZnO nanorods (NRs) grown by low-temperature aqueous chemical growth method and a p-type Polyfluorene (PF) organic film fabricated by spin-coating. The results indicate that densely and uniformly distributed ZnO nanorods were successfully grown on the PF layer. The thickness of the PF layer plays a dominant role for the current–voltage (I-V) characteristic of the ZnO NRs/PF inorganic-organic hybrid junction device, and a p-n junction with obviously rectifying behavior was achieved with optimal PF layer thickness. The photoluminescence (PL) spectrum covering the broad visible range was obtained from the n-ZnO nanorods/p-polyfluorene (PF) structure, which was originated from the combination of the PF-related blue emission and the ZnO-related deep level emission.

1. Introduction

Recently, white-light emitting diode (LED) is triggering a revolution of general illumination. As a novel, convenient and low-cost approach to straightforward white-light electroluminescence, the inorganic-organic hybrid junction devices are being studied extensively around the world, which take advantage of the high carrier mobility of inorganic materials and the high luminescence efficiency of organic materials at very low cost [1-3]. Among the numerous inorganic semiconductors, ZnO is a very promising inorganic material suitable for a wide range of applications due to its wide and direct band gap and large exciton binding energy [4]. In particular, ZnO nanostructures have currently got more interests due to the large surface area to volume ratio, quantum size effect as well as the their self organized growth on almost any substrates regardless of the lattice mismatch between ZnO and the substrate [5]. So far, there have been several reports on the realization of electroluminescence from ZnO based inorganic-organic heterojunction nanostructures [6-8]. However, most emissions are from either ZnO only [2,8] or the organic layer only [3]. Bright white-light electroluminescence was recently achieved from ZnO nanorod (NR)/polyfluorene (PF) inorganic-organic heterojunction light-emitting diodes (LEDs), confirming the ZnO NR/PF inorganic-organic

heterojunction is very promising for developing high brightness straightforward white-light emitting diodes [9]. An important and key issue for the development and application of such inorganic-organic hybrid junction devices is to realize the controllable growth for desired functionality. Therefore, fundamental understanding of the effects of preparation parameters and carrier transport mechanism of such ZnO NR based inorganic-organic hybrid junction devices are desirable and essential.

In our very recent studies, controllable growth of well-aligned ZnO NRs with high optical quality was successfully achieved by low-temperature aqueous chemical growth method via adjusting the preparation parameters [5]. Low-temperature aqueous chemical growth method has been proven to be a high performance growth technique for ZnO NRs, due to its excellent advantages such as low cost, low temperature, non-toxic operation and environmental friendliness. There are different options of the choice for the p-type polymers to be combined with n-type ZnO NRs to form the inorganic-organic hybrid junction devices [10-12]. Among the possible candidates, PF are novel and promising blue light emitting materials with extremely high efficiency. In addition, the advantage of using PF polymer was the possibility of growing the ZnO NRs by low temperature approaches on

large substrates and hence the potential of developing large area white light emitting sources.

In this work, the inorganic-organic hybrid junction with n-ZnO nanorods/p-polyfluorene (PF) structure was grown with low-temperature aqueous chemical growth method. The results indicate that densely and uniformly distributed ZnO nanorods were successfully grown on the PF layer, and a p-n junction with reasonable rectifying behavior was formed at the interface between ZnO NR inorganic layer and PF organic layer. White-light photoluminescence was achieved by combining the PF-related blue emission with ZnO-related deep level emission.

2. Experiment

The ZnO NR/PF inorganic-organic hybrid junction device was designed and schematically illustrated in Fig. (1a), in which the ZnO NRs and the organic film served as the n- and p-type component, respectively. Polyfluorene (PF) was used as the organic layer and spin-coated on ITO glass substrate to serve as p-type layer, then, a very thin ZnO seeds layer (~30nm) was deposited on the as-grown PF layer to facilitate vertically aligned nanorods by radio frequency (RF) magnetron sputtering with Ar used as the working gas. The Ar flow rate, RF power, and chamber pressure were maintained at 15 SCCM, 180 W, and 3.5 Pa, respectively. Subsequently, ZnO NRs were grown on ZnO seeds layer from an aqueous solution composed of 0.025mol/L zinc acetate $(Zn(CH_3COO)_2 \cdot 2H_2O$, reagent-grade) and hexamethylenetetramine (HMT) $(C_6H_{12}N_4$, analytic-grade) with a ration of 1:1 at a low temperature of 95°C for 5h in a sealed container. A detailed process for ZnO NRs growth by low-temperature aqueous chemical growth method has been described elsewhere [13]. After growth, the samples were cooled down to room temperature naturally, rinsed thoroughly in deionized water, and dried in air, and then embedded in an insulating PMMA layer that is spin coated from PMMA solution. The PMMA layer in the device is used to provide isolation for the individual ZnO NRs and prevent direct contact between the PF and the top electrode. The thickness of PMMA was accurately controlled to expose the tip of ZnO nanorod for metallization. To ensure good contacts of each layer, the sample is then annealed at 100°C for 30 min to remove the residual solvent. Finally, an aluminum layer is deposited by a conventional thermal evaporation through a shadow mask with bar shape hollow out to provide a contact for electron injection. The detailed device fabrication processes are schematically shown in Fig. (1b).
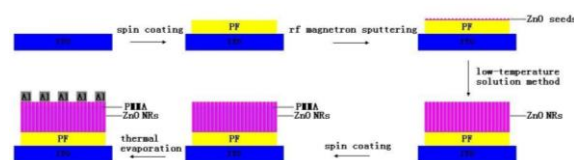

Fig. (1) (a) Schematic diagram of detailed ZnO NRs/PF inorganic-organic hybrid junction device fabrication processing procedure

Field emission scanning electron microscope (FE-SEM) was used to investigate the morphology of the as-grown structure on HITACHI S-4800. To investigate the electrical properties of the ZnO NRs/PF inorganic-organic hybrid junction device, the current–voltage (I-V) characteristic measurements were carried out using a Keithley 2611A semiconductor diode parameter analyzer. To investigate the optical properties, PL measurements were performed at room temperature by a Jobin Yvon HR320 spectrometer using a He–Cd laser (30mW) with an excitation wavelength of 325 nm.

3. Results and Discussion
3.1 Microstructure and morphology

Figure (2a) shows the SEM cross-section image of as-grown ZnO NRs grown on ITO substrate. It can be clearly observed from the figure that the ZnO well-defined nanorods array was successfully grown densely and vertically on the substrate, and the average diameter of the ZnO nanorods is 120nm. Figure (2b) shows the SEM image of as-grown ZnO NRs grown on PF thin films after PMMA embedding, inset is a magnified image.
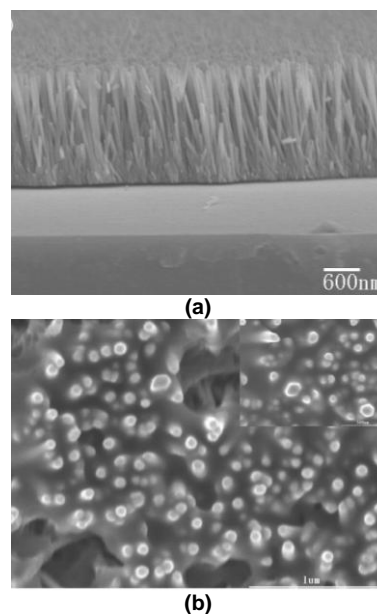

Fig. (2) (a) shows the SEM cross-section image of as-grown ZnO NRs grown on ITO substrate. (b) shows the SEM image of as-grown ZnO NRs grown on PF thin films after PMMA embedding, inset is a magnified image

The bright spots are the ZnO NRs and the dark area is the space between the NRs filled with PMMA. Therefore, it indicates that a thin PMMA coating on top of the ZnO NRs with a suitable thickness can be achieved, and the space between the ZnO NRs is solidly filled with PMMA to effectively prevent short-circuit between individual ZnO NRs. Moreover, it s clearly observed that some of the ZnO NRs tips are not covered with the PMMA insulating layer, allowing the possibility to contact them with electrodes. The relatively poor homogeneity can be understood considering the fact that not all the ZnO nanorods have the same height. This implies that it is necessary to optimize the growth process in order to obtain ZnO nanorods having the same height so more efficient LED can be achieved, since more ZnO nanorods will be contributing to the emission.

3.2 Optical properties

The photoluminescence (PL) was performed to investigate the optical emission and access the quality of our grown PF thin film and ZnO NRs.b To distinguish the peaks origination in the fabricated structure, the PL characteristics of the ZnO NR/PF hybrid structures were measured at room temperature before and after the growth of the ZnO NRs. Figure (3) shows the PL spectra of ZnO NR/PF hybrid structures before (Fig. 3a) and after (Fig. 3b) the growth of ZnO nanorods.

In Fig. (3a), two intensity peaks and a broad band were observed centered at 422nm, 438nm, and 527nm, respectively, which corresponds to the PF polymer material as expected [9]. The blue emission of PF polymer is originating from excitonic emission and its vibronic progression from non-interacting single chains.

In Fig. (3b), similar characteristics with Fig. (3a) can be clearly identified. Comparing Fig. (3a) with Fig. (3b), it can be observed that the PF-related blue emission peaks have shifted from 422nm and 438nm in Fig. (3a) to 438nm and 465nm in Fig. (3b), after the growth of ZnO NRs on PF polymer layer. The red-shift of PF-related blue emission could be attribute to the instability and impurity of PF polymer material [14,15]. In addition, the vanish of ZnO-related near band edge UV emission (~380 nm) and superposition of the broad deep level emission (DLE) band of ZnO NRs implies that, in current ZnO NR/PF configuration, the PL intensity of PF is much stronger than that of ZnO NRs [16]. It is known that the peak position can be different in different samples due to the fact that the DLE is a superposition of different contributions from specific defect related bands [17,18]. However, the obvious difference between Fig. (3a) and Fig. (3b) provided convincing evidence that the grown ZnO NRs have contributed observable emission in the visible region of the ZnO NR/PF hybrid structure as expected. It is important to mention that the hybrid organic

inorganic white light structure discussed above, can utilize the different emission possibilities in organic LEDs, e.g., exciton emission, excipler emission, and together with the DLE form the ZnO nanorods [19].
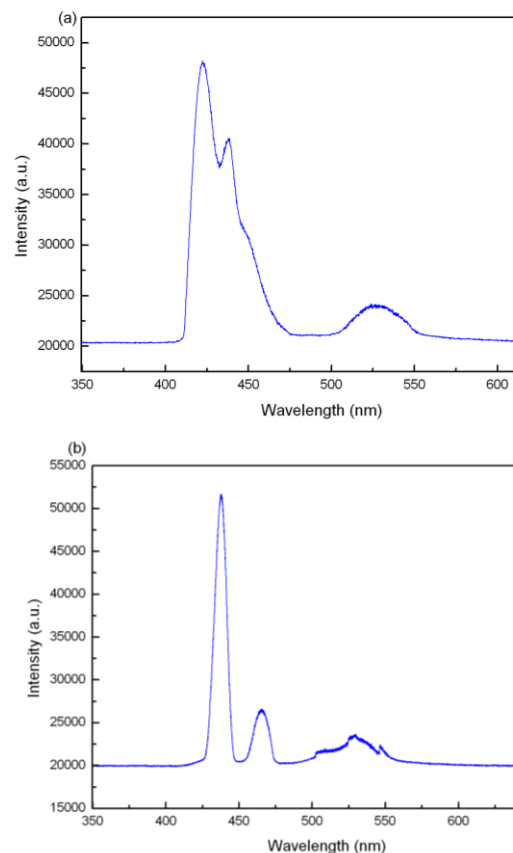

Fig. (3) The room temperature PL spectra of the ZnO NRs/PF hybrid structures before (a) and after (b) the growth of the ZnO nanorods

3.3 Electrical properties

As direct Hall Effect measurements to obtain reliable electrical properties of individual layer of the ZnO NRs/PF hybrid structure are difficult to accomplish, because the extremely high resistance for PF film and the necessary 2D configuration of the Hall contacts is hard to achieve for ZnO NRs. A simple and reliable method to investigate the electrical properties of the ZnO NRs/PF hybrid structure is to study the current transport mechanism via I-V characteristic. Fig.4 represents the typical I-V characteristic for ZnO NRs/PF heterojunction at room temperature (RT). Three kinds of device with different structures, ITO/PF/Al (device A), ITO/PF/ZnO NRs:PMMA/Al (device B), ITO/ZnO NRs:PMMA/Al (device C), were fabricated for comparison, and their cut-in voltages are about 5V, 6V, and 8V, respectively. For the PF single-layer device (device A), it has been found that the thickness of the PF layer play a dominant role for the I-V characteristic of the obtained device. If the PF thin film is too thin, the devices will breakover. When the PF thin film is too thick, the rectification characteristic will degrade. The optimized PF thin

film thickness is found to be around 80nm.

Figure (4) shows the I-V curve for the PF single-layer device (device A) with optimized PF thin film thickness in terms of rectification characteristic. While for the ZnO NRs single-layer device (device C), a symmetrical I-V characteristic is obtained. That is to say, the potential barrier between ITO and ZnO NRs is similar to that between ZnO NRs and Al. It also indicates that the ZnO NRs directly contact the ITO substrate would lead to the large current leakage. This finding is similar to previous report by C.Y. Lee [9].
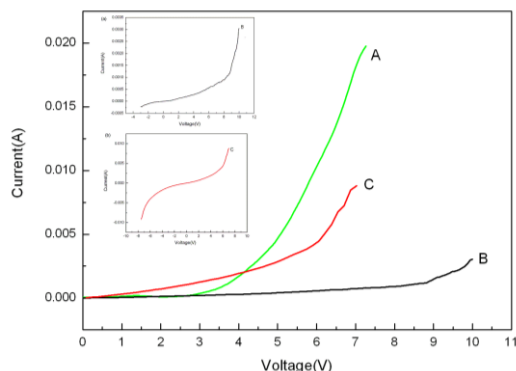

Fig. (4) The room temperature I-V curves of device A, B, and C. Insets (a) and (b) are room temperature I-V curves of device B and C, respectively

For the PF/ZnO NRs double-layer structure, a reasonable p-n junction characteristic is demonstrated. The value of the ideality factor was roughly estimated to be in the range 3~4. The higher value of the ideality factor indicates that the transport mechanism is no longer dominated by the thermoionic emission. Non ideal behavior is often attributed to defect states in the band gap of the semiconductor or at the interface providing other current transport mechanisms such as structural defects, surface contamination, barrier tunneling or generation recombination in the space charge region and to variations in interface composition. In our case, a much high density defect states are supposed to be present at the interface between ZnO NR inorganic layer and PF organic layer due to the large lattice mismatch and the extremely low growth temperature. Compare with the single layer devices of PF thin film and ZnO NRs, the PF/ZnO NRs double-layer has a smaller current. The reason could be related to the residual PMMA isolated layer on top of ZnO NRs, but further investigations are certainly needed.

4. Conclusions

In this paper, the n-ZnO NRs/p-PF inorganic-organic hybrid structure are suggested as a solution to avoid the well known ZnO p-type doping

difficulties and still utilize the potential of ZnO for optoelectronic appliance. The results indicated that densely and uniformly distributed ZnO nanorods were successfully grown on the PF layer, and a p-n junction with obviously rectifying behavior was formed at the interface between ZnO NR inorganic layer and PF organic layer. A photoluminescence (PL) spectra covering the broad visible range was achieved from the n-ZnO nanorods/p-polyfluorene (PF) structure, which was resulted from the combination of the blue PF-related emission and the ZnO-related deep level emission. The achievement of the n-ZnO NRs/p-PF inorganic-organic hybrid junction reported in this work should provide a convenient and low-cost route toward the realization of ZnO-based white-light EL devices with low-temperature processes in the future.

References

[1] A. Wadeasa, O. Nur, and M. Willander, *Nanotechnology*, 20(6) (2009), 065710-1-5.
[2] X.W. Sun et al., *Nano Lett.*, 8(4) (2008) 1219-1223.
[3] J.Z. Huang et al., *Solid State Commun.*, 142(7) (2007) 417-420.
[4] L. Schmidt-Mende and J.L. MacManus-Driscoll, *Mater. Today*, 10(5) (2007) 40-48.
[5] Q.W. Li et al., *Appl. Surf. Sci.*, 256(6) (2010) 1698-1702.
[6] A. Wadeasa et al., *Phys. Lett.*, 490(4-6) (2010) 200-204.
[7] H.Y. Li et al., *J. Nanopart. Res.*, 3(2-3) (2001) 157-160.
[8] R. Ko1nenkamp, R.C. Word, and M. Godinez, *Nano Lett.*, 5(10) (2005) 2005-2008.
[9] C.Y. Lee et al., *Nanotechnology,* 20(42) (2009) 425202-1-5.
[10] J.H. Na et al., *Appl. Phys. Lett.*, 95(25) (2009) 253303-1-3.
[11] A. Zainelabdin et al., *Nanoscale Res. Lett.*, 5(9) (2010) 1442-1448.
[12] M. Willander et al., *Materials*, 3(4) (2010) 2643-2667.
[13] Y. Sun et al., *J. Phys. Chem. C*, 112(25) (2008) 9234-9239.
[14] L. Liu and X.D. Chen, *Ind.*, 32(4) (2004) 18-20.
[15] L.Q. Chen and X.Y. Qu, *J. South-Central University for Nationalities*, 26(4) (2007) 5-9.
[16] Y.Z. Lu et al., *Chin. J. Lumin.*, 30(4) (2009) 495-498.
[17] Ü. Özgür et al., *J. Appl. Phys.*, 98(4) (2005) 041301-1-103.
[18] T. Moe Børseth et al., *Appl. Phys. Lett.,* 89(26) (2006) 262112-1-3.
[19] M. Willander et al., *New J. Phys.,* 11 (2009) 125020-1-16.

THE IRAQI JOURNAL OF
APPLIED PHYSICS
EDITORIAL BOARD

COPYRIGHT RELEASE FORM
IRAQI JOURNAL OF APPLIED PHYSICS (IJAP)

We, the undersigned, the author/authors of the article titled
……
……
……
……
……
that is presented to the Iraqi Journal of Applied Physics (IJAP) for publication, declare that we have neither taken part or full text from any published work by others, nor presented or published it elsewhere in any other journal. We also declare transferring copyrights and conduct of this article to the Iraqi Journal of Applied Physics (IJAP) after accepting it for publication.

The authors will keep the following rights:
1. Possession of the article such as patent rights.
2. Free of charge use of the article or part of it in any future work by the authors such as books and lecture notes without referring to the IJAP.
3. Republishing the article for any personal purposes of the authors after taking journal permission.

To be signed by all authors:

Signature:…………………………………………………………….date: …………………………………………
Printed name: ……………………………………………………………………………………………………..……

Signature:…………………………………………………………….date: …………………………………………
Printed name: ………

Signature:…………………………………………………………….date: …………………………………………
Printed name: ………

Correspondence address:……………………………………………………………………………………………...
………
Address:……
………
Telephone:……………………….…………………..email: ……………………………………………………….....

Note: Please complete and sign this form and mail it to the below address with your manuscript

The Iraqi Journal of Applied Physics
P. O. Box 55259, Baghdad 12001, IRAQ
Email: irq_appl_phys@yahoo.com, editor_ijap@yahoo.co.uk
Phone: +964 7901274190

IRAQI JOURNAL OF APPLIED PHYSICS
Volume (9), Issue (1), January - March 2013

CONTENTS